The Astrophysical Journal, 928:31 (16pp), 2022 March 20 https://doi.org/10.3847/1538-4357/ac4605

Significant Dust-obscured Star Formation in Luminous Lyman-break Galaxies at $z \sim 7$–8

Sander Schouws[1], Mauro Stefanon[1], Rychard Bouwens[1], Renske Smit[2], Jacqueline Hodge[1], Ivo Labbé[3], Hiddo Algera[1], Leindert Boogaard[1], Stefano Carniani[4], Yoshinobu Fudamoto[5,6], Benne W. Holwerda[7], Garth D. Illingworth[8], Roberto Maiolino[9,10,11], Michael Maseda[12], Pascal Oesch[13,14], and Paul van der Werf[1]
[1] Leiden Observatory, Leiden University, NL-2300 RA Leiden, The Netherlands
[2] Cavendish Laboratory, University of Cambridge, 19 JJ Thomson Avenue, Cambridge CB3 0HE, UK
[3] Centre for Astrophysics and SuperComputing, Swinburne, University of Technology, Hawthorn, Victoria, 3122, Australia
[4] Scuola Normale Superiore, Piazza dei Cavalieri 7, I-56126 Pisa, Italy
[5] Research Institute for Science and Engineering, Waseda University, 3-4-1 Okubo, Shinjuku, Tokyo 169-8555, Japan
[6] National Astronomical Observatory of Japan, 2-21-1, Osawa, Mitaka, Tokyo, Japan
[7] Department of Physics and Astronomy, University of Louisville, Natural Science 102, Louisville, KY 40292, USA
[8] UCO/Lick Observatory, University of California, Santa Cruz, 1156 High Street, Santa Cruz, CA 95064, USA
[9] Cavendish Laboratory, University of Cambridge, 19 J.J. Thomson Avenue, Cambridge CB3 0HE, UK
[10] Kavli Institute for Cosmology, University of Cambridge, Madingley Road, Cambridge CB3 0HA, UK
[11] Department of Physics and Astronomy, University College London, Gower Street, London WC1E 6BT, UK
[12] Department of Astronomy, University of Wisconsin-Madison, 475 N. Charter Street, Madison, WI 53706 USA
[13] Departement dAstronomie, Université de Genéeve, 51 Ch. des Maillettes, CH-1290 Versoix, Switzerland
[14] International Associate, Cosmic Dawn Center (DAWN), Niels Bohr Institute, University of Copenhagen and DTU-Space, Technical University of Denmark, Denmark
Received 2021 May 24; revised 2021 December 10; accepted 2021 December 11; published 2022 March 24

Abstract

We make use of Atacama Large Millimeter/submillimeter Array continuum observations of 15 luminous Lyman-break galaxies at $z \sim 7$–8 to probe their dust-obscured star formation. These observations are sensitive enough to probe obscured star formation rates (SFRs) of 20 $M_\odot$ yr^{-1} (3σ). Six of the targeted galaxies show significant ($\geqslant 3\sigma$) dust-continuum detections, more than doubling the number of known dust-detected galaxies at $z > 6.5$. Their IR luminosities range from 2.7×10^{11} $L_\odot$ to 1.1×10^{12} $L_\odot$, equivalent to obscured SFRs of 25 to 101 $M_\odot$ yr^{-1}. We use our results to quantify the correlation of the infrared excess (IRX) on the UV-continuum slope $\beta_{\rm UV}$ and stellar mass. Our results are most consistent with a Small Magellanic Cloud (SMC) attenuation curve for intrinsic UV-slopes $\beta_{\rm UV,intr}$ of -2.63 and most consistent with an attenuation curve in between SMC and Calzetti for $\beta_{\rm UV,intr}$ slopes of -2.23, assuming a dust temperature T_d of 50 K. Our fiducial IRX–stellar mass results at $z \sim 7$–8 are consistent with marginal evolution from $z \sim 0$. We then show how both results depend on T_d. For our six dust-detected sources, we estimate their dust masses and find that they are consistent with dust production from supernovae if the dust destruction is low (<90%). Finally we determine the contribution of dust-obscured star formation to the SFR density for UV luminous ($H < -21.5$ mag: $\gtrsim 1.7$ $L^*_{\rm UV}$) $z \sim 7$–8 galaxies, finding that the total SFR density at $z \sim 7$ and $z \sim 8$ from bright galaxies is $0.20^{+0.10}_{-0.10}$ dex and $0.23^{+0.06}_{-0.09}$ dex higher, respectively; i.e., $\sim\frac{1}{3}$ of the star formation in $\gtrsim 1.7$ $L^*_{\rm UV}$ galaxies at $z \sim 7$–8 is obscured by dust.

Unified Astronomy Thesaurus concepts: High-redshift galaxies (734); Galaxies (573); Lyman-break galaxies (979); Interstellar dust (836); Interstellar dust extinction (837); Galaxy evolution (594)

1. Introduction

One major uncertainty in our understanding of galaxy formation during the Reionization Epoch concerns the role of early dust build-up. Deep surveys in the rest-frame UV with both ground- and space-based facilities have enabled the identification of large samples of galaxies at $z > 2$ and measurement of their UV-based star formation rates (SFRs) up to redshift $z \sim 11$ (e.g., Bouwens et al. 2011, 2014, 2015, 2016a, 2017; Ellis et al. 2012; Laporte et al. 2012; McLure et al. 2013; Schenker et al. 2013; Finkelstein et al. 2015; McLeod et al. 2016; Kawamata et al. 2018; Oesch et al. 2014, 2015, 2018). The rest-frame UV view only accounts for unobscured star formation and could be significantly impacted by the presence of dust in galaxies. Fortunately, accurate measurements of the dust-obscured SFRs in galaxies to $z < 3$ have been available for the past ten years, thanks to deep and wide-field far-infrared (FIR) observations from Herschel and Spitzer (Reddy et al. 2006; Daddi et al. 2007; Magnelli et al. 2009, 2013; Magnelli & Decarli 2020; Karim et al. 2011; Cucciati et al. 2012; Schreiber et al. 2015; Álvarez-Márquez et al. 2016).

Less is known however about star formation in $z > 3$ galaxies that might be obscured by dust (e.g., Bouwens et al. 2016b; Dunlop et al. 2016; Casey et al. 2018; Wang et al. 2019; Williams et al. 2019). Because of the limited sensitivity and increasing source confusion suffered by Herschel and Spitzer, the obscured star formation in $z > 3$ galaxies could initially only be studied in the most luminous systems (e.g., Riechers et al. 2013; Oteo et al. 2016; Marrone et al. 2018). Consequently, studies of the SFR density at $z > 3$ often account for the impact of obscured star formation based on the UV light alone. Especially useful in this regard has been the empirical relation between the UV-continuum slope $\beta_{\rm UV}$ and the infrared excess (IRX $= L_{\rm IR}/L_{\rm UV}$). In the local universe, the IRX has been found to show a good correlation with $\beta_{\rm UV}$ for

star-forming galaxies (Meurer et al. 1999; Takeuchi et al. 2010; Overzier et al. 2010; Casey et al. 2014). Moreover, this same correlation seems to hold up to at least $z \sim 3$ (Reddy et al. 2006, 2010, 2011; Daddi et al. 2009; Overzier et al. 2010; Sklias et al. 2014; Pannella et al. 2015; Bouwens et al. 2016b; Álvarez-Márquez et al. 2016; Whitaker et al. 2017; Fudamoto et al. 2017, 2019, 2020; McLure et al. 2018).

The availability of new observations from submillimeter facilities like the Atacama Large Millimeter/submillimeter Array (ALMA) and the NOrthern Extended Millimeter Array (NOEMA), which have much better sensitivity and resolution than previous facilities, have had an especially important impact on studies of obscured star formation and dust in $z > 3$ galaxies (e.g., Hodge & da Cunha 2020). Most importantly, these facilities have enabled the detection of obscured star formation in normal main-sequence star-forming galaxies at $z > 3$ by utilizing deep field observations (Aravena et al. 2016; Aravena & Boogaard 2020; Bouwens et al. 2016b, 2020; Dunlop et al. 2016; McLure et al. 2013) and targeted studies (e.g., Capak et al. 2015; Willott et al. 2015; Knudsen et al. 2017; Laporte et al. 2017; Bowler et al. 2018; Hashimoto et al. 2019; Tamura et al. 2019; Fudamoto et al. 2020), but the majority of observed high-redshift sources remain undetected in the dust continuum (e.g Maiolino et al. 2015; Bouwens et al. 2016b; Carniani et al. 2017, 2018; Smit et al. 2018; Bowler et al. 2018; Matthee et al. 2017, 2019; Hashimoto et al. 2018). This indicates that star formation in normal $z > 3$ galaxies may be less obscured than in the local universe, especially in normal and small galaxies, and previous corrections to the UV derived SFRs to determine the cosmic star formation history may be overestimated (e.g., Bouwens et al. 2016b; Capak et al. 2015; Willott et al. 2015; Barisic et al. 2017; Faisst et al. 2017, 2020; Fudamoto et al. 2017, 2019, 2019). This is corroborated by recent findings from Fudamoto et al. (2020), who found that the IRX of $z \sim 4$–6 galaxies from ALPINE (Le Fèvre et al. 2020) can be much better explained with a steeper attenuation curve like that of the Small Magellanic Cloud (SMC) than with grayer attenuation curves like that of Calzetti.

Despite the significant amount of progress in detecting obscured star formation in galaxies to redshifts $z \sim 6.5$, much less is known about the dust properties and obscured SFRs of galaxies at $z > 6.5$, with only four dust-continuum detections thus far identified in normal star-forming galaxies at $z \sim 7$–8 (Watson et al. 2015; Knudsen et al. 2017; Laporte et al. 2017; Bowler et al. 2018; Hashimoto et al. 2019; Tamura et al. 2019). Additionally, there have also been a modest number of prominent dust-continuum detections in more extreme ULIRG-type (Ultra-Luminous InfraRed Galaxy; defined as $L_{\rm IR} > 10^{12}\ L_{\odot}$) sources (Marrone et al. 2018) and QSOs at $z > 6.5$ (Venemans et al. 2012, 2015a, 2015b, 2017, 2018; Bañados et al. 2015; Mazzucchelli et al. 2017).

Further insight can be obtained into the dust properties of luminous $z > 6$ galaxies by increasing the number of such galaxies targeted with sensitive dust-continuum observations. In this spirit, we successfully proposed for ALMA-continuum observations on a significant sample of luminous $z \sim 8$ galaxies to study the dust-continuum emission from luminous high-redshift galaxies. In addition, we also obtained sensitive ALMA-continuum observations on seven other bright $z \sim 7$ galaxies as part of two other programs aimed at probing the 157.74 μm [C II] line (hereafter $[\mathrm{C\,II}]_{158\mu\mathrm{m}}$). Eight of these galaxies were identified as part of the Stefanon et al. (2017, 2019) study of bright star-forming galaxies at $z \gtrsim 8$ in the Cosmic Evolution Survey (COSMOS)/UltraVISTA field, while the $z \sim 7$ galaxies were primarily part of a similar selection of bright galaxies at $z \sim 7$ (S. Schouws et al. 2021, in preparation). Focus on the brightest and most massive galaxies in the early universe is especially promising for the study of obscured star formation and dust, given the prevalence of dust in such galaxies at lower redshift (e.g., Hodge & da Cunha 2020), and the observability of such sources with ALMA and NOEMA.

In this paper, we make use of these new ALMA-continuum observations to characterize the dust properties of some of the most massive galaxies in the $z \sim 7$–8 universe. Our new observations significantly add to the ALMA-continuum observations currently available for galaxies at $z > 6$, allowing us to quantify in much more detail both the dust emission and obscured star formation in these massive sources. In addition, the new observations allow us to constrain the dust attenuation law for high-redshift sources more accurately and increase the sample of sources where we have estimates of dust masses, which is essential for studying the build-up of dust early after the Big Bang.

The layout of this paper is as follows. In Section 2, we describe both the selection of our sources and the ALMA observations. In Section 3, we present our new ALMA-continuum results and then combine these results with the available UV observations to derive the IR luminosities and IRXs for individual sources. We then use these new measurements to constrain the form of IRX-M_* and IRX-β relations, look at spatial offsets between UV and dust-continuum light. In Section 4, we discuss the constraints on the dust build-up in our galaxies as well as the impact on the cosmic star formation rate density, and finally, in Section 5, we summarize our conclusions. Throughout this paper, we assume a standard cosmology with $H_0 = 70$ km s^{-1} Mpc^{-1}, $\Omega_m = 0.3$, and $\Omega_\Lambda = 0.7$. Magnitudes are presented in the AB system (Oke & Gunn 1983). For SFRs and stellar masses, we adopt a Chabrier initial mass function (IMF; Chabrier 2003).

2. Targets and ALMA Observations

The purpose of this Section is to provide a brief summary of the deep ALMA-continuum observations and bright $z \sim 7$–8 targets we analyze in this study as part of five separate ALMA programs. A summary of the observations we describe in this Section is provided in Table 1.

2.1. ALMA-continuum Observations of Bright z ∼ 7 Galaxies

As part of an effort to better characterize the physical properties of very luminous galaxies at $z \sim 7$, we used an ALMA cycle-6 program (2018.1.00085.S: P.I. Schouws) to observe six luminous $z \sim 7$ galaxies. The observations were designed to use spectral scans to search for the $[\mathrm{C\,ii}]_{158\mu\mathrm{m}}$ line, while simultaneously probing the dust-continuum emission from sources. This paper focuses on the dust-continuum properties of these sources, while we defer the discussion on the $[\mathrm{C\,ii}]_{158\mu\mathrm{m}}$ emission to a companion study (S. Schouws et al. 2021, in preparation). That paper also details the manner in which six bright $z \sim 7$ sources were selected for targeting and our identification of [C II] (signal-to-noise ratio, S/N, > 9) in three of them.

Table 1
Observational Parameters of the ALMA Observations

Source Name	R.A.	Decl.	Beamwidth[a] (arcsec)	Integration Time[b] (min.)	Achieved Sensitivity (μJy: 1σ)	Central Frequency (GHz)	Project Code
			$z\sim7$ Sample				
UVISTA-Z-001	10:00:43.36	02:37:51.3	$1\farcs47\times1\farcs21$	78.36	17.9	234.0	2018.1.00085.S
UVISTA-Z-007	09:58:46.21	02:28:45.8	$1\farcs40\times1\farcs19$	65.52	17.4	245.7	2018.1.00085.S
UVISTA-Z-009	10:01:52.30	02:25:42.3	$1\farcs38\times1\farcs20$	65.52	19.0	245.7	2018.1.00085.S
UVISTA-Z-010	10:00:28.12	01:47:54.5	$1\farcs44\times1\farcs18$	78.36	14.7	234.0	2018.1.00085.S
UVISTA-Z-013	09:59:19.35	02:46:41.3	$1\farcs45\times1\farcs18$	78.36	15.0	234.0	2018.1.00085.S
UVISTA-Z-019	10:00:29.89	01:46:46.4	$1\farcs39\times1\farcs18$	65.52	18.0	245.7	2018.1.00085.S
COS-3018	10:00:30.19	02:15:59.8	$1\farcs63\times1\farcs49$[c]	766.08	7.0	233.5	2017.1.00604.S
			$z\sim8$ Sample				
UVISTA-Y-001	09:57:47.90	02:20:43.7	$1\farcs17\times0\farcs96$	37.50	13.4	203.1	2018.1.00236.S
UVISTA-Y-002	10:02:12.56	02:30:45.7	$1\farcs17\times0\farcs96$	37.50	13.3	203.1	2018.1.00236.S
UVISTA-Y-003	10:00:32.32	01:44:31.3	$0\farcs60\times0\farcs52$	33.26	19.1	230.4	2017.1.01217.S
UVISTA-Y-004	10:00:58.49	01:49:56.0	$1\farcs03\times0\farcs94$	91.73	9.3	231.3	2017.1.01217.S& 2018.A.00022.S
UVISTA-Y-005	10:00:31.89	01:57:50.2	$1\farcs17\times0\farcs96$	37.50	12.9	203.1	2018.1.00236.S
UVISTA-Y-006[f]	10:00:12.51	02:03:00.5	$1\farcs17\times0\farcs96$	37.50	13.2	203.1	2018.1.00236.S
UVISTA-Y-007[d]	09:59:02.57	02:38:06.1	$0\farcs60\times0\farcs53$	34.78	17.9	230.4	2017.1.01217.S
UVISTA-Y-009[e, f]	09:59:09.62	02:45:09.7	$0\farcs60\times0\farcs53$	34.78	17.9	230.4	2017.1.01217.S

Notes.
[a] Beam size as measured in the natural weighted continuum images.
[b] Corresponds to the total integration time in case of multiple tunings. In total, 25.7 hr of integration time on source is included in this analysis.
[c] For this data set, we use a $1\farcs5$ tapered continuum image; the full $\sim0\farcs25$ resolution data will be presented in R. Smit et al. (2021, in preparation).
[d] Source name in ALMA observations is Y8.
[e] Source name in ALMA observations is Y10.
[f] UVISTA-Y-006 and UVISTA-Y-009 are estimated to be magnified by factors of $\sim$0.27 dex and $\sim$0.29 dex, respectively, due to lensing from foreground galaxies (Stefanon et al. 2019). Given the large uncertainty in the lensing magnification factor, the luminosities and fluxes for these sources are not corrected for lensing.

The six sources in the program were identified using the very deep optical, near-IR (NIR), and Spitzer/Infrared Array Camera (IRAC) observations obtained over the 2 deg^2 COSMOS/UltraVISTA field from significant survey programs within COSMOS (Scoville et al. 2007; Capak et al. 2007), Canada-France-Hawaii Telescope Legacy Survey (CFHT-LS; Erben et al. 2009; Hildebrandt et al. 2009), UltraVISTA (McCracken et al. 2012), Spitzer Large Area Survey with Hyper-Suprime-Cam (SPLASH; Capak et al. 2013), and Spitzer Matching Survey of the UltraVISTA ultra-deep Stripes (SMUVS; Caputi et al. 2017; Ashby et al. 2018).

Each of the sources was selected to show a strong break across the Y and z filters ($z-Y>2$ mag), show blue UV-continuum slopes, and show moderately blue or red Spitzer/IRAC [3.6]-[4.5] colors, i.e., <-0.3 or $\geqslant0.3$. Significantly red or blue Spitzer/IRAC colors not only provide evidence for substantial [O III]$_{5007\AA}$+Hβ line emission in the sources (e.g., equivalent widths EW([O III]$_{5007\AA}$+Hβ)$\gtrsim$500 Å; Smit et al. (2015)), but also indicate to which IRAC band the line emission contributes. By combining this information with that available from the Lyman break, accurate redshift constraints can be derived $\Delta z\lesssim0.15$ (see also Smit et al. 2015; Roberts-Borsani et al. 2016) on the six targeted galaxies, making it possible for us to efficiently scan for [C ii]$_{158\mu m}$. A more extensive description of the source selection is included in S. Schouws et al. (2021, in preparation).

All six targets were observed in band-6 as part of ALMA program #2018.1.00085.S using the most compact configuration for maximal sensitivity (C43-1: $\sim1\farcs3$ resolution). The spectral setup was chosen to enable a scan for [C ii]$_{158\mu m}$ over essentially the full frequency range expected on the basis of our precise redshift constraints. We were able to execute this scan using just two separate tunings with three spectral windows each. The full bandwidth for each scan was therefore 10.75 GHz in total. Approximately 40 minutes were required in each tuning to reach a sensitivity of 0.25 mJy per 66 km s^{-1}, which was chosen to ensure detection of [C II]$_{158\mu m}$ based on previous studies (e.g., Smit et al. 2018). The precipitable water vapor during the executed observations ranged from 1.6 to 3.5 mm. We refer to Table 1 for a detailed overview of the parameters of our observations.

Additionally, we also utilize the sensitive, higher spatial resolution band-6 observations we obtained of $z=6.853$ source COS-3018555981 (Smit et al. 2018; hereafter abbreviated to COS-3018). The purpose of those observations was to characterize in detail the kinematics of a $z\sim7$ galaxy with a relatively luminous [C ii]$_{158\mu m}$ line and to determine if the kinematics were more consistent with simple rotation or a merging system. COS-3018 was one of two $z\sim6.8$ sources featured in Smit et al. (2018) and found to show prominent differential motion across the detected [C ii]$_{158\mu m}$ profile. Thanks to the depth of the band-6 observations on this source, these observations can also be used to characterize the IRX in this source.

In interpreting the ALMA results obtained for our $z\sim7$ galaxy targets, it is worthwhile asking whether our selection criteria for our targets might bias our results. After all, our selection of $z\sim7$ targets required that their [O III]$_{5007\AA}$+Hβ nebular emission lines be sufficiently strong to narrow the redshift likelihood distribution for sources. As we will discuss in S. Schouws et al. (2021, in preparation), the median source in our $z\sim7$ selection only had a [O III]$_{5007\AA}$+Hβ EW of

$\sim$1000 Å. Since this is roughly consistent with the median EW (759^{+112}_{-113} Å) derived by Endsley et al. (2021) for the $z \sim 7$ population of luminous galaxies, we can conclude that our $z \sim 7$ results appear to be representative.

2.2. ALMA-continuum Observations of Bright z $\sim$ 8 Galaxies

We additionally targeted the eight most luminous Lyman-break galaxies at $z \sim 8$ in UltraVISTA to obtain sensitive continuum constraints on their far-IR emission and obscured star formation. The targeted sources were identified as part of a search for bright Lyman-break galaxies at $z \sim 8$ (Stefanon et al. 2017, 2019), where sources were required to have $Y - (J + H)/2$ colors redder than 0.75 mag, to show a blue UV-continuum slope redward of the Balmer break, and a low probability of being a low-redshift galaxy based on spectral energy distribution (SED) fits.

The eight sources were targeted as part of two ALMA programs #2017.1.01217.S (P.I. Stefanon) and #2018.1.00236.S (P.I. Stefanon) and observed for $\sim$35 minutes each. To optimize the probability for detection for $[\mathrm{C\,II}]_{158\mu\mathrm{m}}$, we used band-6 to obtain continuum observations of those sources whose best-fit photometric redshifts were $z < 8$ and band-5 to obtain continuum observations for those whose best-fit redshifts were $z > 8$. As a result of the relatively large photometric redshift uncertainties on the Stefanon et al. (2019) $z \sim 8$ sources and the cost of pursuing spectral scans, we elected to use a single spectral setup to maximize the continuum sensitivity. We also obtained 58 minutes of follow-up observations (#2018.A.00022.S: P.I. Schouws) on one source from ALMA program #2017.1.01217, UVISTA-Y-004, in an effort to confirm a tentative 2.5σ dust-continuum detection of that source.

We note that two sources from in sample, UVISTA-Y-006 and UVISTA-Y-009, are estimated to be magnified by factors of $\sim$0.27 dex and $\sim$0.29 dex, respectively, due to lensing from foreground galaxies (Stefanon et al. 2019). However, the exact value of the magnification factor is relatively uncertain and model dependent. We also note that lensing does not impact our measurement of IRX because this is defined as a ratio of two luminosities that are magnified by the same factor. The impact of differential lensing is likely minimal due to the minimal offsets we observe between the dust-continuum and rest-frame UV emission (typically $<0\farcs2$; see Section 3.3), which are much smaller than the distances to the lensing galaxies ($>3''$; Stefanon et al. 2019). Moreover, both sources are not detected in the continuum and therefore do not impact our discussion on the mechanisms of dust build-up (see Sections 3 and 4). We therefore do not explicitly correct the fluxes and luminosities of these sources to account for the magnification.

2.3. ALMA Data Reduction

The ALMA data were reduced and calibrated using CASA version 5.4.1 following the standard ALMA pipeline procedures. The imaging was performed using the TCLEAN task in CASA, applying natural weighting to maximize signal-to-noise. Any channels containing line emission from the $[\mathrm{C\,II}]_{158\mu\mathrm{m}}$ line were carefully excluded from the continuum imaging. All significant continuum sources in the field were masked and cleaned conservatively to 3σ. A range of *(u,v)*-tapers from 1.0″ to 2.0″ were applied, but it was found that the images without any *(u,v)*-tapering had the highest S/N. Therefore we use the setup without any *(u,v)*-tapering for the remainder of this paper unless specified otherwise. We reduce the observations for COS-3018 in a similar way except applying a $1\farcs5$ taper to the visibility data; the full-resolution results will be presented in R. Smit et al. (2021, in preparation).

To examine in more detail the relative morphologies of galaxies in terms of their far-IR dust-continuum emission and in the rest-frame UV, we also re-imaged the sources using Briggs weighting with robustness parameter 0.3, where a robustness parameter of -2 corresponds to uniform weighting (which maximizes the spatial resolution of the continuum signal) and 2 to natural weighting (which maximizes the S/N). Our choice of 0.3 for the robustness parameter was made as a compromise between resolution and S/N. In particular, for the most luminous source (UVISTA-Y-003), we used Briggs weighting to decrease the size of our beam from $0\farcs60 \times 0\farcs52$ to $0\farcs45 \times 0\farcs37$. This is useful to constrain the physical alignment between the UV and FIR, which will be further discussed in Section 3.3.

2.4. Near-IR Imaging Observations

In interpreting the dust-continuum observations for our $z \sim 7$–8 sources, it is helpful to compare against the sensitive imaging observations that are available for these targets in the NIR. All 14 of our targets have available sensitive $YJHK_s$ imaging observations from the UltraVISTA program, albeit with limited ($\mathrm{FWHM}_{PSF} \sim 0\farcs8$) spatial resolution. For a few sources, higher spatial resolution imaging observations exist from the Hubble Space Telescope (HST), in particular for UVISTA-Z-001 (one orbit in F140W; Bowler et al. 2017), UVISTA-Y-003 (one orbit in F160W, Drift-and-Shift (DASH; Momcheva et al. 2016) and COS-3018 (1.3 orbits in F160W, Cosmic Assembly Near-infrared Deep Extragalactic Legacy Survey (CANDELS); Grogin et al. 2011).

To ensure good registration of the available NIR observations with our new ALMA-continuum observations, we took advantage of the high astrometric accuracy of the GAIA DR2 catalog (Gaia Collaboration et al. 2018) to make minor ($<0\farcs1$) adjustments to the astrometry of the NIR imaging observations available for the COSMOS field from UltraVISTA or HST (if available). As a further check on the astrometric accuracy of the NIR imaging data, we compared the position of eight lower-redshift dust-continuum detections in our ALMA data with their position in the NIR imaging data and found good agreement ($<0\farcs2$).

3. Results

3.1. Individual Detections

The new ALMA observations we have obtained on a significant sample of 15 bright $z \sim 7$–8 galaxies provide us with essential new information on the obscured star formation and dust-continuum emission in these sources.

Using natural weighted reductions of the continuum observations, we performed a systematic search for 3σ peaks within 1″ of the rest-frame UV positions of our 15 targeted sources. We find a significant dust-continuum detection for six of the sources, as is illustrated in Figure 1, which shows the 2σ, 3σ, 4σ, 5σ, and 6σ dust-continuum contours overlaid on the rest-frame UV emission. The continuum detections show $<0\farcs5$ spatial offsets from the UV positions. We note that allowing for

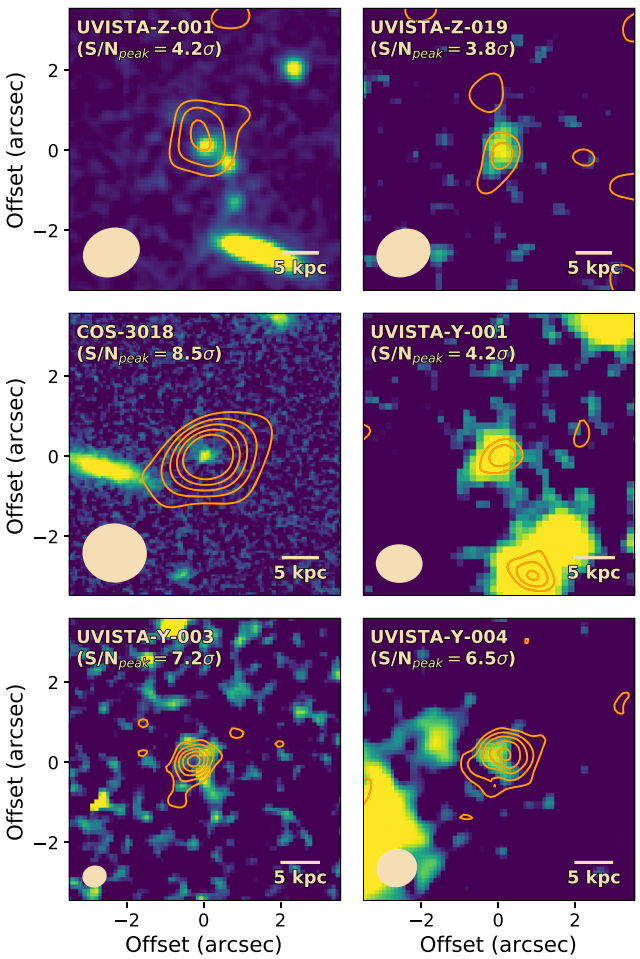

Figure 1. An overlay of band-6 dust-continuum observations (1.2 μm) with ALMA on the available NIR imaging observations for six $z \sim 7$–8 sources detected in the dust continuum. For UVISTA-Z-001, UVISTA-Y-003, and COS-3018, NIR imaging observations are from one orbit HST F140W, F160W, and F160W exposures, respectively, and for the remaining sources, from stacked J + H + K$_s$ imaging from UltraVISTA. Contours are drawn at (2, 3, 4, 5, 6) $\times \sigma$ using the sensitivities from Table 1 (typically $\sigma \approx 15$ μJy beam^{-1}). The ALMA contours presented here are from the natural weighted imaging, except for COS-3018 where a 1.″5 taper is used (see Section 2.3). The synthesized beam for the dust-continuum observations is indicated in the lower-left corner of each panel. The significance of the dust detections for each source is stated below the source name (peak S/N). In Figure 12, we show the continuum results for sources lacking a clear detection.

large spatial offsets (e.g., to 3″) does not increase the number of detected sources.

To measure continuum fluxes for the detected sources, the complex visibilities were fitted using UVMULTIFIT (Martí-Vidal et al. 2014), applying a 2D Gaussian model with a single component. By fitting in the *(u,v)*-plane, the results are independent of the imaging parameters. The fluxes measured in this way are consistent with measurements in the image plane, and measured fluxes range from 75^{+6}_{-10} μJy to 302^{+45}_{-35} μJy, comparable with previous studies at $z \gtrsim 7$ (Watson et al. 2015; Willott et al. 2015; Laporte et al. 2017; Knudsen et al. 2017; Bowler et al. 2018; Tamura et al. 2019; Hashimoto et al. 2019). In the case of non-detections, we provide 3σ upper limits derived from the noise measured in the natural weighted imaging. For convenience, we summarize the results in Table 2. The fluxes in this Table have not been corrected for effects arising from the cosmic microwave background (CMB). For derived quantities ($L_{\rm IR}$, $M_{\rm dust}$, etc.), we correct the measured fluxes for the reduced contrast due to the higher temperature of the CMB at high redshifts using Equation (18) of da Cunha et al. (2013).

For comparison with other results in the literature and lower-redshift studies, it is convenient to estimate the total infrared luminosities for the sources in our sample. Following previous studies, we adopt a modified single-temperature blackbody dust SED and integrate the SED between 8 and 1000 μm to calculate $L_{\rm IR}$. For the dust emissivity index, we assume $\beta_d = 1.6$, which is the best-fitting value for local infrared luminous galaxies (Casey et al. 2014).

Dust temperatures in typical star-forming galaxies in the local universe are around ~35 K (Casey et al. 2014; Rémy-Ruyer et al. 2015), but it has been shown using stacking of Herschel observations that dust temperatures increase with redshift (Béthermin et al. 2015; Schreiber et al. 2015, 2018; Faisst et al. 2017, 2020). Other observational (e.g., Bouwens et al. 2016b; Coppin et al. 2014; Knudsen et al. 2017; Capak et al. 2015; Watson et al. 2015; Bouwens et al. 2020) and theoretical (Behrens et al. 2018; Liang et al. 2019; Sommovigo et al. 2021) studies also suggest such a trend. We note however that there seems to be a large scatter in the dust temperatures at high redshift, with evidence for very hot ($T > 80$ K; Bakx et al. 2020; Laporte et al. 2019) and relatively cold temperatures ($T \sim 25$ K; Harikane et al. 2020) in individual sources. We therefore adopt a dust temperature of 50 K for our analysis (this is the dust temperature after any CMB heating).

To put our dust-continuum detections in context, we show the IR luminosities we have inferred for the sources in our samples against redshift in Figure 2 and then compare these detections with IR luminosities inferred for other dust-detected galaxies at $z > 6$. Interestingly enough, one of our $z > 7$ galaxies has an IR luminosity in excess of 10^{12} $L_\odot$, which places the source in the ULIRG category and is the most IR-luminous galaxy known at $z > 7$. For context, we have also estimated the limiting luminosities to which we would have succeeded in detecting bright $z \sim 7$ and $z \sim 8$ galaxies, given the integration times for sources in the two samples.

We estimate SFR$_{\rm UV}$ and SFR$_{\rm IR}$ for sources following Madau & Dickinson (2014), with conversion factors SFR$_{\rm UV}$ = $\kappa_{\rm UV} \cdot L_{\rm UV}$ and SFR$_{\rm IR}$ = $\kappa_{\rm IR} \cdot L_{\rm IR}$ where $\kappa_{\rm UV} = 2.5 \cdot 10^{-10}$ $M_\odot yr^{-1} L_\odot^{-1}$ and $\kappa_{\rm IR} = 1.73 \cdot 10^{-10} M_\odot yr^{-1} L_\odot^{-1}$, and we convert from a Salpeter IMF to Chabrier IMF with SFR$_{\rm Cha}$ = 0.63 $\cdot$ SFR$_{\rm Sal}$ (Madau & Dickinson 2014). We compare these SFR estimates for our sources to previous detections and upper limits at $z > 6.5$ (Ota et al. 2014; Maiolino et al. 2015; Watson et al. 2015; Pentericci et al. 2016; Inoue et al. 2016; Knudsen et al. 2017; Bradač et al. 2017; Laporte et al. 2017; Bowler et al. 2018; Carniani et al. 2018; Hashimoto et al. 2018; Smit et al. 2018; Hashimoto et al. 2019; Tamura et al. 2019; Matthee et al. 2019) in Figure 3.

Interestingly enough, we find that the obscured SFRs (SFR$_{\rm IR}$) for sources are fairly similar to the unobscured SFRs (SFR$_{\rm UV}$), in cases where the dust is detected. This is consistent with previous results in the literature, which include a few prominent detections where SFR$_{\rm IR}$ > SFR$_{\rm UV}$ (Knudsen et al. 2017; Laporte et al. 2017; Bowler et al. 2018; Hashimoto et al. 2019; Tamura et al. 2019) and many sources that lack prominent dust detections and SFR$_{\rm IR}$ < SFR$_{\rm UV}$ (Ota et al. 2014; Maiolino et al. 2015; Watson et al. 2015; Pentericci et al. 2016; Matthee et al. 2017, 2019).

Table 2
Physical and Measured Characteristics of the Bright $z \sim 7$–8 Galaxies Targeted with ALMA Observations

Source Name	Redshift[a]	$m_{\rm UV}$	$\beta_{\rm UV}$[b]	$L_{\rm UV}$ (10^{11} $L_\odot$)	$\log(M_*)$[b] ($M_\odot$)	S_ν[d] (μJy)	$L_{\rm IR}$[f] (10^{11} $L_\odot$)
UVISTA-Z-001	7.0611[c]	23.9 ± 0.1	$-1.88^{+0.22}_{-0.07}$	$2.9^{+0.1}_{-0.1}$	$9.58^{+0.09}_{-0.35}$	104^{+43}_{-43}	$5.0^{+2.1}_{-2.1}$
UVISTA-Z-007	6.7498[c]	24.5 ± 0.1	$-2.02^{+0.22}_{-0.22}$	$1.5^{+0.2}_{-0.2}$	$9.57^{+0.35}_{-0.44}$	<52.2	<2.2
UVISTA-Z-009	$6.90^{+0.10}_{-0.06}$	24.6 ± 0.1	$-1.88^{+0.21}_{-0.51}$	$1.6^{+0.2}_{-0.2}$	$9.40^{+0.32}_{-0.29}$	<57.0	<2.4
UVISTA-Z-010	$7.07^{+0.09}_{-0.07}$	24.6 ± 0.1	$-2.39^{+0.35}_{-0.28}$	$1.1^{+0.2}_{-0.2}$	$8.88^{+0.28}_{-0.09}$	<44.1	<2.1
UVISTA-Z-013	$7.02^{+0.06}_{-0.02}$	24.9 ± 0.2	$-2.24^{+0.36}_{-0.15}$	$1.4^{+0.4}_{-0.3}$	$10.72^{+0.03}_{-0.10}$	<45.0	<2.2
UVISTA-Z-019	6.7544[c]	25.1 ± 0.2	$-1.51^{+0.29}_{-0.15}$	$1.0^{+0.1}_{-0.1}$	$9.51^{+0.19}_{-0.18}$	66^{+23}_{-23}	$2.7^{+0.9}_{-0.9}$
COS-3018	6.8540[c]	24.9 ± 0.1	$-1.22^{+0.51}_{-0.51}$	$1.3^{+0.1}_{-0.1}$	$9.14^{+0.18}_{-0.06}$	65^{+13}_{-13}	$3.0^{+0.6}_{-0.6}$
UVISTA-Y-001	$8.53^{+0.53}_{-0.62}$	24.8 ± 0.1	$-1.37^{+0.36}_{-0.44}$	$2.1^{+0.3}_{-0.3}$	$10.0^{+0.9}_{-0.4}$	73^{+20}_{-20}	$3.5^{+1.0}_{-1.0}$
UVISTA-Y-002	$8.21^{+0.50}_{-0.49}$	24.8 ± 0.2	$-2.60^{+0.58}_{-0.51}$	$1.9^{+0.4}_{-0.3}$	$9.0^{+0.3}_{-1.2}$	<39.9	<2.3
UVISTA-Y-003	$7.62^{+0.14}_{-0.28}$	25.0 ± 0.1	$-1.88^{+0.80}_{-0.73}$	$1.3^{+0.2}_{-0.2}$	$9.9^{+0.6}_{-0.3}$	241^{+30}_{-30}	$10.7^{+1.3}_{-1.3}$
UVISTA-Y-004	$7.42^{+0.19}_{-0.20}$	24.9 ± 0.2	$-1.80^{+0.29}_{-0.29}$	$1.5^{+0.4}_{-0.3}$	$9.9^{+0.5}_{-0.2}$	65^{+17}_{-17}	$2.9^{+0.8}_{-0.8}$
UVISTA-Y-005	$8.60^{+0.58}_{-0.65}$	24.9 ± 0.2	$-1.59^{+1.24}_{-0.58}$	$1.8^{+0.5}_{-0.4}$	$9.0^{+0.4}_{-1.1}$	<38.7	<2.5
UVISTA-Y-006	$8.32^{+0.66}_{-0.92}$	25.3 ± 0.3	$-1.70^{+0.70}_{-0.80}$	$1.2^{+0.3}_{-0.3}$	$9.7^{+1.1}_{-0.5}$	<39.6	<2.5
UVISTA-Y-007	$8.47^{+0.73}_{-0.72}$	25.5 ± 0.3	$-2.00^{+0.70}_{-0.50}$	$1.1^{+0.4}_{-0.3}$	—[g]	<53.7	<2.5
UVISTA-Y-009	$7.69^{+0.99}_{-0.71}$	25.4 ± 0.3	$-2.60^{+0.90}_{-0.60}$	$1.0^{+0.4}_{-0.3}$	—[g]	<53.6	<2.5
Stack at $z \sim 7$[e]	$6.95^{+0.07}_{-0.08}$	24.6 ± 0.2	$-1.99^{+0.25}_{-0.25}$	$1.5^{+0.2}_{-0.2}$	$9.6^{+0.6}_{-0.4}$	33^{+21}_{-24}	$1.4^{+1.0}_{-1.0}$
Stack at $z \sim 8$[e]	$7.87^{+0.20}_{-0.23}$	25.1 ± 0.2	$-2.13^{+0.21}_{-0.21}$	$1.5^{+0.1}_{-0.1}$	$9.3^{+0.5}_{-0.9}$	27^{+14}_{-12}	$1.3^{+0.6}_{-0.5}$
Stackof non − detections	$7.72^{+0.40}_{-0.42}$	24.9 ± 0.2	$-2.16^{+0.22}_{-0.22}$	$1.4^{+0.3}_{-0.3}$	$9.2^{+0.3}_{-0.7}$	<23.5	<1.2

Notes.
[a] Quoted redshifts are based on the photometric redshift estimates given in S. Schouws et al. (2021, in preparation) or Stefanon et al. (2019).
[b] UV-continuum slopes $\beta_{\rm UV}$ and stellar masses are from Stefanon et al. (2019) or use the methodology described in Stefanon et al. (2019) for these estimates, assuming a 0.2 $Z_\odot$ metallicity, a constant star formation prescription, and a Calzetti et al. (2000) dust law.
[c] Spectroscopic redshifts are from the $[\rm C\ II]_{158\mu m}$ line (S. Schouws et al. 2021, in preparation and Smit et al. (2018) for COS-3018).
[d] Integrated flux derived with UVMULTIFIT (not corrected for CMB effects: see Section 3.1). Upper limits on non-detections are 3σ.
[e] Stack fluxes and errors are determined using a bootstrapping analysis (see Section 3.2).
[f] Total infrared luminosity integrated from 8 to 1000 μm assuming a modified blackbody SED with a dust temperature of 50 K and a dust emissivity index $\beta_{\rm dust} = 1.6$ after correcting for CMB effects (see Section 3.1).
[g] Due to the challenges in measuring the flux of these sources in the Spitzer/IRAC data caused by confusion from bright neighboring sources (Stefanon et al. 2019), no stellar masses are estimated for these sources.

The IRX ($\rm IRX = L_{IR}/L_{UV}$) is discussed in detail in Sections 3.4 and 3.5, but we note here that for equal obscured and unobscured SFRs ($\rm SFR_{UV} = SFR_{IR}$), $\log_{10}(\rm IRX) = 0.10$. The derived $\log_{10}(\rm IRX)$ increases or decreases by 1.0 for corresponding factor-of-10 increases and decreases, respectively, in the obscured SFR relative to the unobscured SFR.

3.2. Stacking Analysis

Nine of the bright $z \sim 7$–8 galaxies targeted by our ALMA programs are not individually detected in our continuum observations. To better characterize dust-continuum emission and obscured star formation in these sources, we can combine the continuum observations on these sources to obtain an average constraint through median-stacking. In addition to stacking those sources that are individually undetected, we repeat the stacking analysis using our entire $z \sim 7$ and $z \sim 8$ samples separately (i.e., both detections and non-detections), to constrain the properties of the hypothetical average galaxy in each sample.

For the stacking, we center sources according to their apparent position in the available HST or UltraVISTA rest-frame UV observations and co-add the ALMA-continuum observations after tapering the continuum images with a $1''$ taper and weighting the sources equally. We use tapered images to ensure that we capture all of the dust-continuum flux and to decrease the impact of both (1) the varying resolutions of the ALMA beam and (2) possible offsets between the dust continuum and UV emission on the stack. This is most relevant for the sources that were observed with a smaller beam, i.e., $< 1''$.

The results of the stack of the nine non-detections are presented in both Table 2 and Figure 4 (left panel). No significant ($<2\sigma$ where $\sigma = 11.8$ μJy) detection is found, which translates to a 3σ upper limit of 1.2×10^{11} $L_\odot$ (assuming $T = 50$ K and $\beta_d = 1.6$) on the IR luminosities of the undetected sources (the stack is also not detected when stacking using a noise-weighted mean). In Table 2 and Figure 4, we also present our stack results for our $z \sim 7$ and $z \sim 8$ samples. A stack of our $z \sim 7$ sample shows a 3.0σ detection, and a stack of our $z \sim 8$ sample shows a 3.8σ detection. The mean IR luminosities we infer for bright $z \sim 7$ and $z \sim 8$ are $1.4^{+1.0}_{-1.0} \times 10^{11}$ $L_\odot$ and $1.3^{+0.6}_{-0.5} \times 10^{11}$ $L_\odot$, respectively. These results and those presented in Table 2 are derived based on a bootstrap resampling procedure, re-stacking subsets with replacement of our sources 10.000×, and using the median peak flux measured in the stacked images. The uncertainties are based on the derived 68% spread in the stack results.

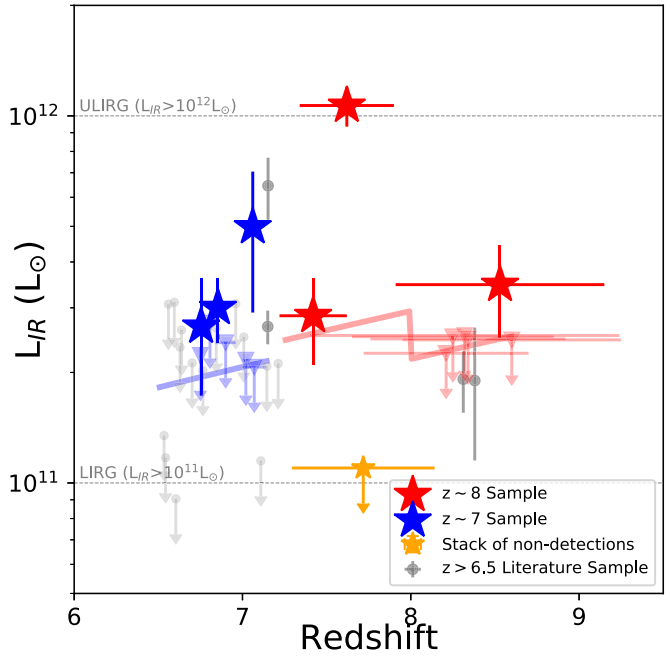

Figure 2. IR luminosities and redshifts for $z \sim 7$ and $z \sim 8$ galaxies detected in ALMA-continuum observations analyzed here (blue and red stars, respectively). The redshifts at which sources are shown are either from detected [C ii]$_{158\mu m}$ lines (S. Schouws et al. 2021, in preparation) or from the computed photometric redshifts. The blue and red plotted downward-pointing triangles correspond to 3σ upper limits on the IR luminosities for the four $z \sim 7$ and five $z \sim 8$ sources undetected in our ALMA observations. Also shown are previous dust-continuum detections from the literature at $z > 6$ (solid gray circles; Watson et al. 2015; Laporte et al. 2017; Bowler et al. 2018; Tamura et al. 2019)) and upper limits (gray arrows; Bradač et al. 2017; Ota et al. 2014; Matthee et al. 2017, 2019; Pentericci et al. 2016; Maiolino et al. 2015; Hashimoto et al. 2018). The thick blue and red lines show the 3σ-limiting IR luminosities we probe given the integration times for our ALMA observations.

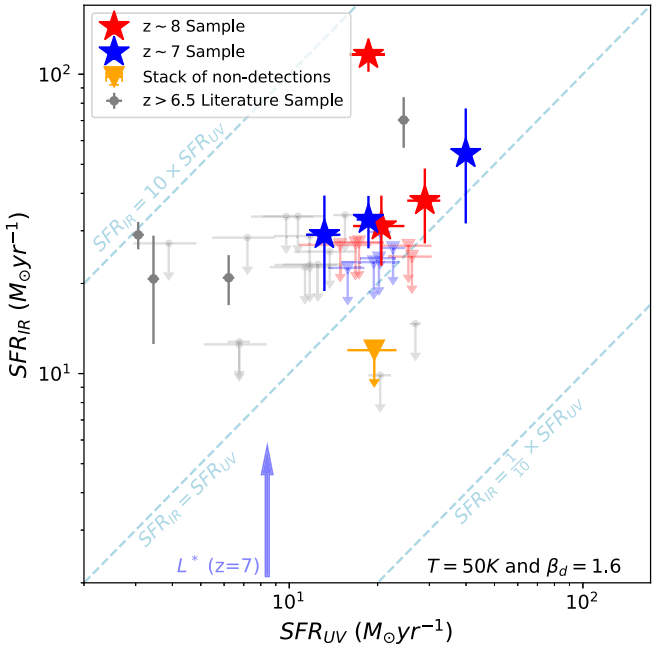

Figure 3. A comparison of the unobscured (SFR_{UV}) and obscured (SFR_{IR}) SFRs inferred from our observations of luminous $z \sim 7$ and $z \sim 8$ galaxies (blue and red colored stars and upper limits, respectively). Previous results for $z > 6.5$ galaxies are shown with the gray symbols and upper limits (see Figure 2 for references). Upper limits are 3σ. For reference, the typical UV SFR of L^* galaxies at $z = 7$ (Bouwens et al. 2015) is indicated with the blue arrow. For the UV luminous sources we analyzed here, the obscured SFRs appear to be comparable to the unobscured SFRs.

3.3. Physical Alignment between UV and FIR

An important longstanding question regards the possible presence of spatial offsets between the dust-continuum emission and the rest-frame UV emission, as have frequently been found when considering IR-luminous galaxies (Smail et al. 2014; Aravena et al. 2016; Dunlop et al. 2016; Laporte et al. 2019). Indeed, one would expect significant spatial offsets between rest-frame UV and IR-continuum emission in galaxies with a nonuniform dust covering fraction, especially when the optical depths become non-negligible. Such offsets can complicate the interpretation of the IRX, which assumes co-spatial emission, and impact SED-fitting codes that assume energy-balancing. Cormier et al. (2019) found evidence for such nonuniform covering fractions in local dwarf galaxies, which are often considered to be good analogs for high-redshift galaxies.

To investigate whether similar spatial offsets are found among the bright $z \sim 7$–8 galaxies we observe with ALMA, we reimage the sources using Briggs weighting, as described in Section 2.3, with a beam of $0\farcs45 \times 0\farcs37$ to examine sources at higher spatial resolution. Figure 5 illustrates how our most prominent dust-continuum detection UVISTA-Y-003 compares to the available rest-frame UV imaging from HST. We show the results for the remaining detections in Appendix B (with the exception of COS-3018, which will be presented in a separate paper; R. Smit et al. 2021, in preparation).

For the majority of our sources, the UV and FIR continuum seem well aligned, with no major offsets between the UV and IR positions (typically smaller than $<0\farcs2$). However, UVISTA-Y-003 is a notable exception, showing an offset of $\sim 0\farcs3$ ($\sim$2 kpc; see Figure 5). Furthermore, for this source, the rest-frame UV emission seems to be divided into three separate clumps, each of which are offset from the dust emission. The UV clumps are discussed in more detail in Stefanon et al. (2019), who performed simulations to assess the robustness of the clumps and also confirmed high-z solutions for the clumps based on deblended photometry. Because of these offsets between the UV clumps and the dust-continuum emission, it seems likely that there is a strongly star-forming region in UVISTA-Y-003, which is almost entirely obscured in the rest-frame UV, similar to what is observed in ULIRGs at $z \sim 0$ and $z \sim 1$–3. It is unclear whether the three rest-frame UV components indicate the presence of merging activity or not. It is worth emphasizing the value of the high-resolution space-based imaging for UVISTA-Y-003 in revealing both the clumpy nature of this source and the offset between the UV and dust-continuum emission.

3.4. Infrared Excess versus UV-continuum Slope

The measured IRX in galaxies ($\mathrm{IRX} = L_{\mathrm{IR}}/L_{\mathrm{UV}}$) is well established to show a correlation with the UV-continuum slope β_{UV} (where $f_\lambda \propto \lambda^{\beta_{\mathrm{UV}}}$). Meurer et al. (1999) showed that the correlation between the IRX and β_{UV} could be expressed as follows:

$$A_{1600} = \frac{dA_{\mathrm{UV}}}{d\beta_{\mathrm{UV}}} \cdot (\beta_{\mathrm{UV}} - \beta_{\mathrm{UV,intr}}) \quad (1)$$

$$\mathrm{IRX} = 1.7 \cdot (10^{0.4 \cdot A_{1600}} - 1) \quad (2)$$

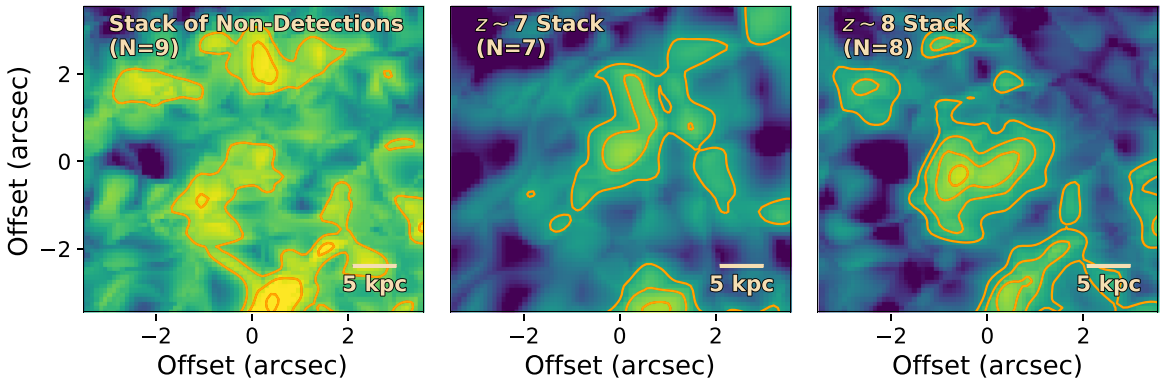

Figure 4. Left: median-stacking of all non-detections (number of sources in the stack; $N = 9$) does not result in a significant detection of the dust continuum. Contours are drawn at (1, 2, 3, 4, 5, 6) $\times \sigma$ where $\sigma = 7.8$ μJy beam^{-1}. Middle and right: median stacks combining the ALMA observations for all $z \sim 7$ (middle, $N = 7$) and $z \sim 8$ (right, $N = 8$) galaxies from our sample (including detections and non-detections) to study the typical properties of our sample. These stacks are marginally detected at 3.0σ ($\sigma = 8.5$ μJy beam^{-1}) and 3.8σ ($\sigma = 6.9$ μJy beam^{-1}), respectively (peak S/N). See Sections 3.2 and 4.2 for a discussion of these results.

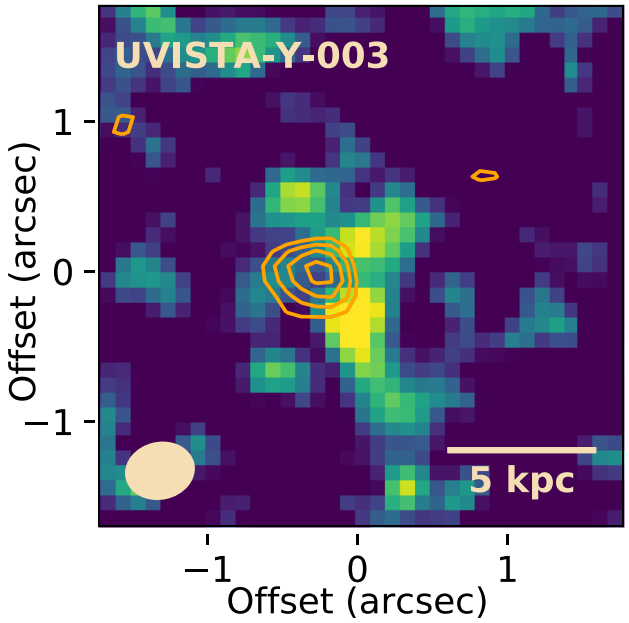

Figure 5. Higher spatial resolution image of the dust-continuum emission from the bright $z \sim 8$ galaxy UVISTA-Y-003 shown relative to the rest-frame UV imaging we have of the source with HST in the F160W band (1.6 μm; $\sim$1900 Å rest frame; $3\farcs5 \times 3\farcs5$ field of view). The presented imaging of UVISTA-Y-003 used a Briggs weighting with robustness parameter 0.3 to bring out the high-spatial resolution structure (Beam: $0\farcs45 \times 0\farcs37$). Contours are drawn at (2.0, 2.5, 3.0, 3.5) $\times \sigma$ where $\sigma = 23$ μJy. Interestingly enough, the UV-continuum emission from UVISTA-Y-003 appears to be divided into three separate clumps (see Stefanon et al. 2019). All of these rest-frame UV clumps show a clear spatial offset from the dust-continuum emission. It therefore seems very likely that there is a high star formation region in UVISTA-Y-003, which is entirely obscured in the rest-frame UV, much like one commonly observes in ULIRGs at both $z \sim 0$ and $z \sim 1$–3. It is unclear whether the multiple rest-frame UV components are indicative of merger activity or clumpy star-forming regions.

where $dA_{\rm UV}/d\beta_{\rm UV}$ expresses the steepness of the attenuation law, $\beta_{\rm UV,intr}$ represents the unattenuated UV-continuum slope of star-forming galaxies, and A_{1600} is the UV attenuation at 1600 Å (Meurer et al. 1999). The IRX–β relation has been used as a constraint on the dust attenuation curve of galaxies. In the local universe, starburst galaxies have been shown (Meurer et al. 1999) to be well described by a Calzetti attenuation law (Calzetti et al. 2000), with $dA_{\rm UV}/d\beta_{\rm UV} = 1.99$ with $\beta_{\rm UV,intr} = -2.23$. However, subsequent studies have found that some galaxies at higher redshifts do not follow the Calzetti dust law and tend to favor a steeper attenuation curve, similar to the SMC for which $dA_{\rm UV}/d\beta_{\rm UV} = 1.1$ and $\beta_{\rm UV,intr} = -2.23$ (Reddy et al. 2006, 2018; Siana et al. 2008; Capak et al. 2015; Bouwens et al. 2016b; Barisic et al. 2017; Fudamoto et al. 2020).

In Figure 6, we present our measurements for the IRX versus the UV-continuum slope ($\beta_{\rm UV}$) for $z > 6.5$ sources with new measurements from our ALMA programs. For this Figure we assume that the rest-frame UV and dust-continuum emission are co-spatial, which is consistent with the lack of significant spatial offsets that can be constrained based on the current data as discussed in Section 3.3. An exception is UVISTA-Y-003, which seems to have a clumpy structure, and we note that treating these clumps individually could significantly impact the interpretation of the IRX–β relation. While the current data are not ideal for constraining the properties of individual clumps, future high-resolution studies with ALMA (project code: 2021.1.01603.S, PI: Hodge) and the James Webb Space Telescope (Stefanon et al. 2021) of this source should enable a more detailed investigation of the individual clump properties.

In determining the best-fit value for $dA_{\rm UV}/d\beta_{\rm UV}$, we consider two different values for $\beta_{\rm UV,intr}$: (1) $\beta_{\rm UV,intr} = -2.23$, as used in modeling the IRX-β relation at $z \sim 0$ (Meurer et al. 1999) and (2) $\beta_{\rm UV,intr} = -2.63$, as expected for a younger, lower-metallicity stellar population (Reddy et al. 2018) seen at higher redshift. For these two values of $\beta_{\rm UV,intr}$, we determine the best-fit value for $dA_{\rm UV}/d\beta_{\rm UV}$ for a dust temperature of 50 K and dust emissivity index $\beta_d = 1.6$. For these fits, we use the detections and non-detections described in this paper and a compilation from the literature ($M_{\rm UV} < -21.5$; Maiolino et al. 2015; Pentericci et al. 2016; Inoue et al. 2016; Matthee et al. 2017, 2019; Hashimoto et al. 2019) assuming the same temperature ($T = 50$ K) for every source in the sample. We determine the best-fit value and errors using a total least-squares method, which takes account of errors in both dependent and independent parameters. To account for non-detections, we measure the maximum peak flux in a 1″ radius around the UV-centroid position following Béthermin et al. (2020) and use those flux measurement in the minimalization routine. To test the robustness of our treatment of upper limits, we furthermore use a Monte Carlo bootstrap method where we draw random flux measurements from the

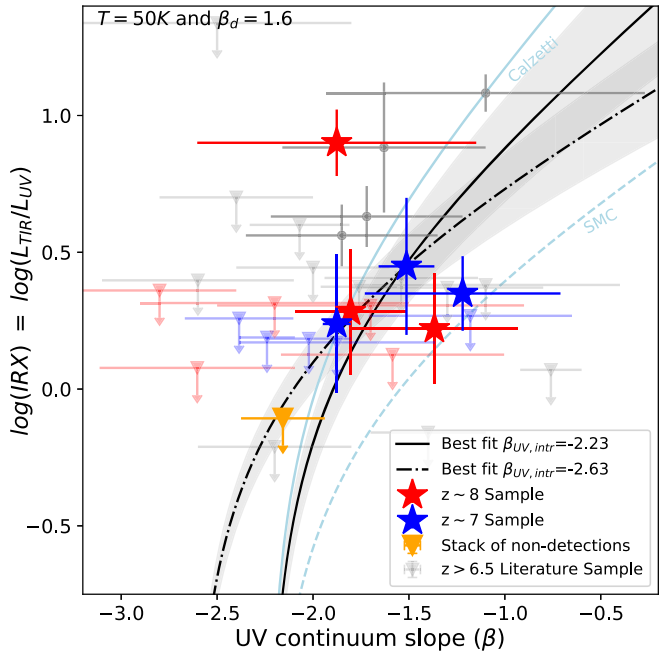

Figure 6. The inferred IRX of $z > 6.5$ galaxies against their UV-continuum slope $\beta_{\rm UV}$. The three blue and three red stars show the IRXs inferred for the $z \sim 7$ and $z \sim 8$ galaxies that are detected in the dust continuum. The blue and red downward-pointing triangles show the 3σ upper limits on the inferred IRX in the eight $z \sim 7$ and $z \sim 8$ galaxies, respectively, lacking dust-continuum detections. The orange downward-pointing triangle shows the 3σ upper limit we infer on the IRX stacking the individually undetected $z \sim 7$–8 galaxies considered here. The gray circles and downward-pointing triangles correspond to dust-continuum detections from the literature (see Figure 2 for references). For reference, the Calzetti and SMC IRX–β relations are shown with the cyan solid and dashed lines, respectively (assuming an intrinsic UV-continuum slope $\beta_{\rm UV}$ of -2.23).

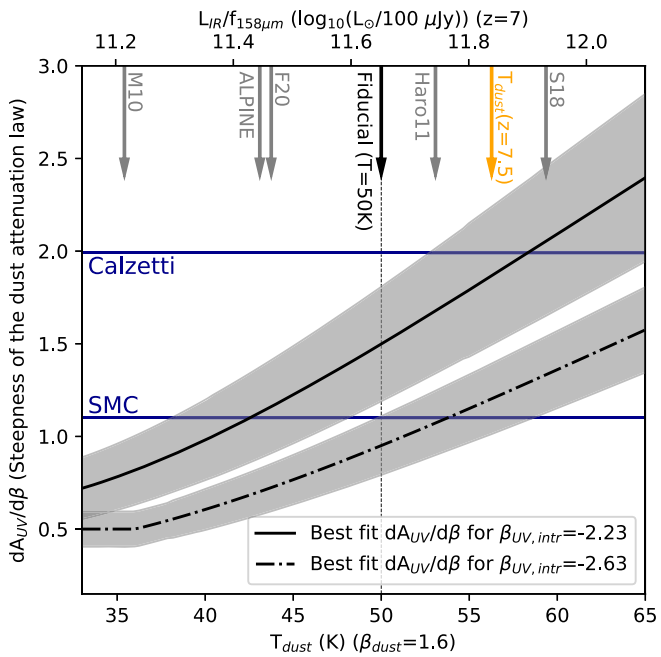

Figure 7. Dependence of the slope parameter of the IRX–β relation ($dA_{\rm UV}/d\beta_{\rm UV}$) on (luminosity-weighted) dust temperature for two different values for the intrinsic UV-continuum slope $\beta_{\rm UV,intr}$ (solid and dashed–dotted black lines). The gray regions show the slopes $dA_{\rm UV}/d\beta_{\rm UV}$ preferred at 68% confidence. The fit uses all detections and upper limits presented in this paper and the literature ($z > 6.5$ and $M_{\rm UV} < -21.5$: $\gtrsim 1.7 L^*_{\rm UV}$). The blue lines indicate a reference to the slope of the SMC and Calzetti relations, while the orange arrow shows the expected dust temperature of Lyman-break galaxies at $z \sim 7$–8 extrapolating dust temperature results in the literature (Bouwens et al. 2020). The gray arrows shown along the top x-axis indicate the $L_{\rm IR}/f_{158\mu m}$ conversion factors (at $z = 7$) for a variety of high-redshift dust SED templates from the literature and at the corresponding temperature of the modified blackbody that has the same conversion factor. Here M10 denotes the FIR-SED model from Michałowski et al. (2010), ALPINE denotes the model from Béthermin et al. (2020), F20 denotes that from Faisst et al. (2020), Haro11 denotes that from Rossi et al. (2018), and S18 denotes that from Schreiber et al. (2018). The black arrow and vertical dotted line indicate the fiducial 50 K temperature we adopt for our analysis. For $\beta_{\rm UV,intr} = -2.23$, we find a much better fit of the observational results for an attenuation curve between Calzetti and SMC, and for a $\beta_{\rm UV,intr} = -2.63$, we find a much better fit to an SMC-like attenuation curve.

completeness function. We model the completeness with an error function with $\mu = 4\sigma_{\rm image}$ and $\sigma = 2\sigma_{\rm image}$ where $\sigma_{\rm image}$ is the rms measured from the continuum image, consistent with Béthermin et al. (2020) and H. Inami et al. (2021, in preparation). With these random flux measurements, we repeat the fit 10.000× for each temperature. We find that both methods give consistent results within the uncertainties.

In Figure 7, we generalize the fit results presented in Figure 6 for $dA_{\rm UV}/d\beta_{\rm UV}$ to allow for an arbitrary dust temperature, given the current uncertainties in establishing the typical dust temperatures for $z > 6$ galaxies. The slopes ($dA_{\rm UV}/d\beta_{\rm UV}$) of the SMC and Calzetti attenuation curves are shown with horizontal blue lines. The error on the $dA_{\rm UV}/d\beta_{\rm UV}$ fit is derived from the formal uncertainties from the covariance matrix of the minimalization. In Figure 7, we indicate with a black arrow (and dotted vertical line) the fiducial dust temperature we assume to be 50 K; this is the luminosity-weighted dust temperature. We also indicate with an orange arrow the $T_{\rm dust}$ determination of 54.3 ± 1.6 K that Bouwens et al. (2020) derived by extrapolating the results from Béthermin et al. (2015), Strandet et al. (2016), Knudsen et al. (2017), Schreiber et al. (2018), Hashimoto et al. (2019), Bakx et al. (2020), Béthermin et al. (2020), Harikane et al. (2020), and Faisst et al. (2020). Also shown in Figure 7 are where other high-redshift SED templates would lie (Béthermin et al. 2015; Schreiber et al. 2018; Faisst et al. 2020; Michałowski et al. 2010; Rossi et al. 2018), including Haro11, which has been argued by Rossi et al. (2018) to be a good low-redshift analog for Lyman-break galaxies and has a relatively high dust temperature. Another is the ALPINE SED template (Béthermin et al. 2020), which is based on a stacking analysis of the ALPINE target and analog galaxies fitted to models from Béthermin et al. (2017). The Michałowski et al. (2010) template is based on the average SED from a sample of submillimeter galaxies. Finally we also indicate the approximate conversion factor and dust temperatures found by Faisst et al. (2020) analyzing a small sample of $z \sim 5.5$ galaxies using the Casey et al. (2018) models.

For our fiducial $z \sim 7$ dust temperature of 50 K and assuming $\beta_{\rm UV,intr} = -2.63$, the current results appear to be more consistent (3σ significance) with a SMC-like attenuation law than a Calzetti-like attenuation law, while for a $\beta_{\rm UV,intr} = -2.23$, current results lie somewhere between a Calzetti and SMC-like attenuation law. For much hotter dust temperatures, as suggested by recent observations (Laporte et al. 2019; Bakx et al. 2020), $dA_{\rm UV}/d\beta_{\rm UV}$ would be more consistent with a Cazetti attenuation law. We also explored the impact of scatter (0.1 dex) on the dust temperatures of the sample, instead of assuming a uniform temperature, and found minimal changes ($\lesssim$0.05 dex) to the results. The present results are similar to earlier $z > 6.5$ results by Watson et al. (2015), Laporte et al.

(2017), Knudsen et al. (2017), Bowler et al. (2018), and Tamura et al. (2019), who also found greater consistency with a Calzetti-like attenuation law when assuming $\beta_{\rm UV,intr} = -2.23$.

3.5. IRX–Stellar Mass Relation

The IRX is also known to show a strong correlation with the stellar mass of sources, with an approximately linear power-law dependence on stellar mass (e.g., Bouwens et al. 2016a; Dunlop et al. 2016; McLure et al. 2018). Interestingly enough, little evolution is observed between $z \sim 3$ and $z \sim 0$ in the relationship between the IRX and the stellar mass (Pannella et al. 2015; Bouwens et al. 2016b; Whitaker et al. 2017; McLure et al. 2018).

In Figure 8 (upper panel), we present the IRX we derive for our sources against their inferred stellar masses. The blue and red stars correspond to $z \sim 7$ and $z \sim 8$ galaxies, respectively, detected in the dust-continuum, while the light blue and light red upper limits correspond to sources that are not detected in the dust continuum ($<3\sigma$). The gray circles show dust-continuum detections from the literature. Stellar masses for bright $z \sim 8$ sources in our selection are from Stefanon et al. (2019). Stellar masses for bright $z \sim 7$ sources are inferred using the same SED-fitting assumptions that Stefanon et al. (2019) used at $z \sim 8$, i.e., with a 0.2 $Z_{\odot}$ metallicity, constant SFR, and Calzetti et al. (2000) dust curve. The lower panel in Figure 8 shows the fraction of obscured star formation against stellar mass. Our results seem broadly consistent with the $z \sim 0$ relation presented in Whitaker et al. (2017) given the sizable uncertainties and large number of upper limits.

Similar to Figure 7, we illustrate in Figure 9 how the normalization in the IRX–stellar mass relation depends on the assumed dust temperature of $z \sim 7$–8 galaxies. We quantify the normalization in terms of an offset (in dex) from the low-redshift relation (Whitaker et al. 2017) and fit this offset as a function of dust temperature using the same fitting procedure as described in Section 3.4. As in Figure 7, the vertical orange line indicates the expected temperature for $z \sim 7$–8 galaxies when extrapolating lower-redshift results. At this temperature, the offset we derive is consistent with no evolution from $z \sim 0$. Not surprisingly, for lower and higher values of the dust temperature, the IRX is lower and higher, respectively, than the $z \sim 0$ relation.

4. Discussion

4.1. Constraints on Dust Evolution Models

Our new observations provide constraints on the build-up of dust in early high-redshift galaxies. In addition to the significant impact dust has on the fraction of UV light seen from star-forming galaxies and that re-emitted in the far-infrared, dust can play a critical role in galaxy evolution (Salim & Narayanan 2020). Significantly, the surfaces of dust grains serve as the main production sites of many molecular species and can catalyze the formation of molecular clouds in which star formation takes place (e.g., Gould & Salpeter 1963; Hirashita & Ferrara 2002; Cazaux & Tielens 2004; Yamasawa et al. 2011; Chen et al. 2017). Additionally, dust cooling induces fragmentation inside molecular clouds, which has a significant impact on the stellar IMF (Omukai 2000; Omukai et al. 2005; Schneider et al. 2006).

In Figure 10, we show estimates for the dust masses of our sources as a function of temperature, and a strong dependence on the assumed dust temperature can be clearly seen. We derive

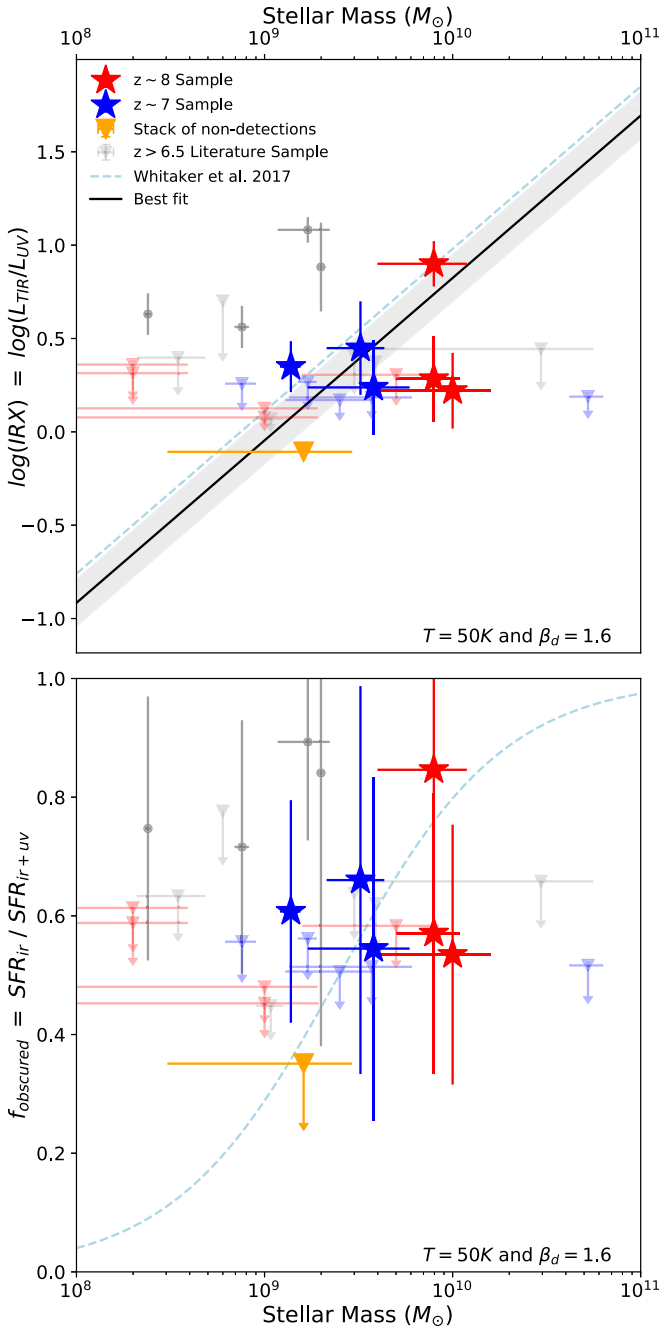

Figure 8. Upper: IRX–stellar mass relation for a sample of sources at $z > 6.5$, including the detections and non-detections presented in this paper and a compilation of sources from the literature (see Figure 2 for references). The local relation (Whitaker et al. 2017) is shown with the dotted line, and our best-fit is shown with the black solid line and the gray-shaded uncertainty. Lower: fraction of the star formation that is obscured by dust as a function of stellar mass for our sample and sources from the literature. For a modified blackbody with a dust temperature of 50 K and a dust emissivity of $\beta_{\rm dust} = 1.6$ (Casey 2012), the $z = 0$ relation (Whitaker et al. 2017) is broadly consistent with the detections seen at high redshift.

our estimates for the dust masses of our sources following the procedure described in Ota et al. (2014):

$$M_{\rm dust} = \frac{S_{\nu_{\rm rest}} D_L^2}{(1+z)\kappa_d(\nu_{\rm rest}) B_{\nu_{\rm rest}}(T_{\rm dust})} \quad (3)$$

where S_ν is the observed flux density after correction for contrast with the CMB (da Cunha et al. 2013; Equation (18)), D_L is the

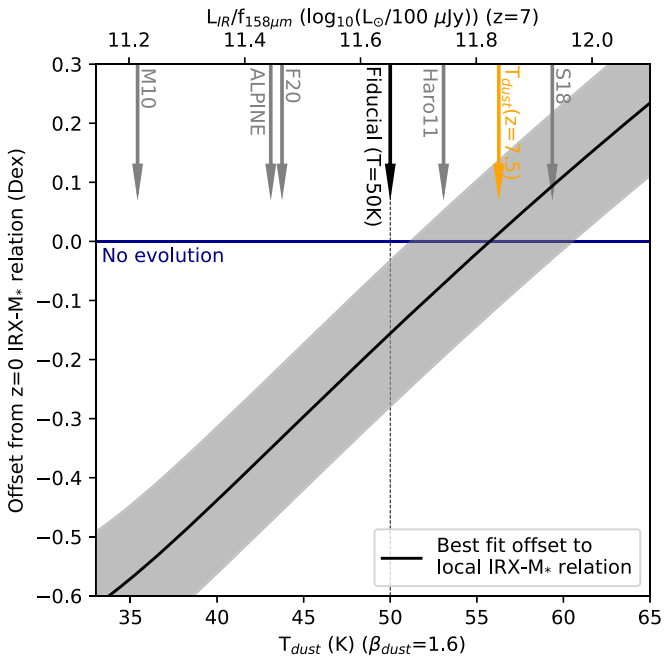

Figure 9. Similar to Figure 7, this Figure shows the dependence on (luminosity-weighted) dust temperature of the offset with respect to the local IRX–stellar mass relation fitted to the detections and upper limits presented in this paper and the literature ($z > 6.5$ and $M_{\rm UV} < -21.5$ mag: $\gtrsim 1.7 L^{*}_{\rm UV}$). The black line shows the best-fit offset while the gray-shaded area shows the offsets preferred at 68% confidence. The blue line is a visual reference corresponding to no evolution. For fit values below this line, the implied IRX at $z > 6.5$ is lower than the local relation at a fixed stellar mass. For the current data, this would be the case for dust temperatures below $\lesssim$54K. The top x-axis and the black, gray, and orange arrows are the same as in Figure 7. For dust temperatures of ∼50–55 K, the present IRX–stellar mass results appear to be broadly consistent with the $z \sim 0$ relation (Whitaker et al. 2017).

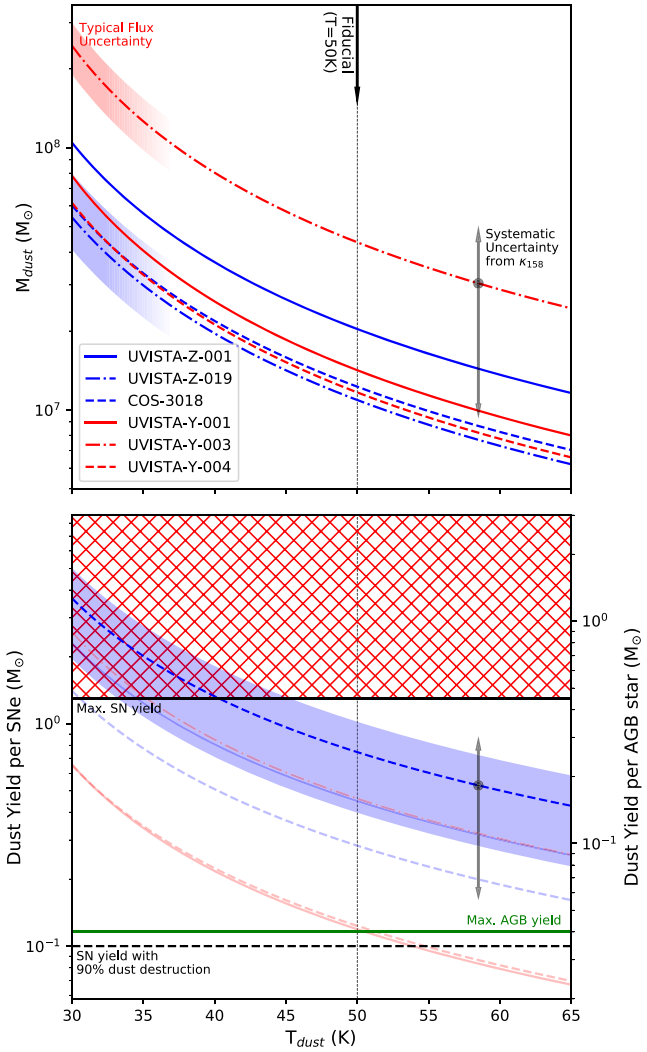

Figure 10. Upper: dust masses as a function of dust temperature. The impact of uncertainties on the flux measurements for the $z \sim 7$ and $z \sim 8$ samples is indicated with the blue and red shaded regions, respectively. An indicative systematic uncertainty resulting from the choice of dust mass absorption coefficient is shown with the black arrow. The dotted vertical line indicates the fiducial dust temperature adopted here. Lower: constraint on the dust yield per SNe (left axis) or asymptotic giant branch (AGB) star (right axis) as a function of temperature for our sources. We highlight COS-3018, which provides the most demanding constraints on the yields, where the blue shaded region shows the error from the flux measurement and the uncertainty in stellar mass. The black arrow indicates the systematic uncertainty resulting from the choice of dust mass absorption coefficient. The maximum theoretical dust yield from SNe without any dust destruction and after 90% dust destruction are indicated with the solid and dashed black lines, respectively. The maximum yield per AGB star is indicated with the green solid line. Note that if the dust yield constraint for a source is above any of these lines, that particular dust production mechanism alone cannot explain the amount of dust we observe. In particular, for dust temperatures below $T \sim 40$ K and our assumed value of κ_{158}, SNe, even without dust destruction, cannot explain the observed dust masses (indicated with the red hatched region).

luminosity distance, $B_\nu(T_{\rm dust})$ is the Planck function at a rest-frame frequency $\nu_{\rm rest}$ and dust temperature $T_{\rm dust}$, and finally $\kappa_d(\nu_{\rm rest})$ is the dust mass absorption coefficient, which scales as $\kappa_d(\nu_{\rm rest}) = \kappa_0(\nu_{\rm rest}/\nu_{\rm ref})^{\beta_{\rm dust}}$. Here we assume $\kappa_0 = 8.94$ cm^2 g^{-1} at 158 μm, which is appropriate for dust ejected from supernovae (SNe) after reverse shock destruction (Hirashita et al. 2014), since it is expected that the majority of dust is produced by SNe (Michałowski 2015; Leśniewska & Michałowski 2019). Alternatively, values ranging from $\kappa_0 = 28.4$ cm^2 g^{-1} at 158 μm for dust consisting of amorphous carbon to $\kappa_0 = 5.57$ cm^2 g^{-1} at 158 μm for dust condensed in SNe before reverse shock destruction (Hirashita et al. 2014) could be considered, leading to an additional ∼0.7 dex systematic uncertainty. Moreover, studies constraining κ_0 directly from observations span a full 3.6 dex range with 0.8 dex scatter (Clark et al. 2019). The impact of these systematic uncertainties (assumed to be 0.7 dex) is shown with the black arrow in Figure 10.

Because our data are observed at ∼158 μm rest frame, which is the same as the reference wavelength of the dust mass absorption coefficient we use from the literature, our choice of $\beta_{\rm dust}$ introduces minimal uncertainty in the derived dust masses. While most of our galaxies appear consistent with dust masses of $\sim 10^7 M_\odot$, the large systematic uncertainty limits us to inferring that the dust mass lies somewhere in the range $\sim 10^7$ $M_\odot$ to 10^8 $M_\odot$ for our sources (assuming $30 < T_{\rm dust} < 65$).

In the lower panel of Figure 10, we use these dust masses in combination with the stellar mass from SED fitting to derive the required dust yields per SNe or asymptotic giant branch (AGB) star following the method described by Michałowski (2015). The stellar mass is translated to the number of SNe or AGB stars that could have contributed to the formation of dust assuming a Chabrier (2003) IMF and a maximum age of 500 Myr (corresponding to a maximum formation redshift of $z \gtrsim 18$; Michałowski 2015). This number is subsequently divided by the dust mass to obtain the required yields.

We compare the required yields for our observed dust masses to the maximum yield from a single AGB star ($\sim$0.004 $M_{\odot}$; Morgan & Edmunds 2003; Ferrarotti & Gail 2006; Ventura et al. 2012; Nanni et al. 2014; Schneider et al. 2014) and a single SN without any dust destruction (approximately $\sim$1.3 $M_{\odot}$; Todini & Ferrara 2001; Nozawa et al. 2003). However, it is likely that a large portion of the dust produced by SNe is destroyed by internal shocks, releasing only $\lesssim 0.1 M_{\odot}$ into the interstellar medium (Bianchi & Schneider 2007; Cherchneff & Dwek 2010; Gall et al. 2011; Lakićević et al. 2015, Ferrara & Peroux 2021).

From this Figure, it is clear that for our sources, dust production from SNe alone could explain the majority of the observed dust, but only when dust destruction is low (less than $\sim$90%). Production from AGB stars by itself (green line) is insufficient to explain the observed dust masses for all dust temperatures. For low dust temperatures $T < 40$ K, even dust production from SNe without any dust destruction would be insufficient, and other mechanism like grain growth (Michałowski 2015; Leśniewska & Michałowski 2019) would be necessary to explain the observed dust masses. Alternatively it is possible that the stellar masses are underestimated, which would lower the required dust yields. Specifically, stellar masses are difficult to measure for sources without a spectroscopic redshift because the rest-frame optical emission as measured from Spitzer IRAC is contaminated by strong nebular emission lines. This contribution is redshift dependent, leading to a 0.6–1.0 dex change in the stellar mass for $\Delta z \sim 0.2$ at $z \sim 7$ (e.g., Schaerer & de Barros 2009; Roberts-Borsani et al. 2020; M. Topping et al., in preparation). Even with spectroscopic redshifts, the contribution of older populations of stars to the stellar mass are difficult to constrain. Rest-frame NIR data would be invaluable to accurately constrain such contributions; however, unfortunately there are currently no instruments that can observe this part of the spectrum with sufficient sensitivity.

4.2. Impact on Measurements of the SFR Density and the IR Luminosity Function at z > 6

The ALMA observations from our programs have particular value in determining the quantity of the star formation from UV-bright galaxies at $z \sim 7$–8 that is obscured by dust. This is particularly useful for gaining a handle on the likely build-up of mass that occurs in the brightest and most massive galaxies with cosmic time.

To estimate the approximate correction that we need to make to the SFR density of bright $z \sim 7$–8 galaxies to correct for the impact of dust, we compute an effective IRX for the entire population of bright $z \sim 7$ and $z \sim 8$ we have targeted as part of multiple programs by dividing the mean $\mathrm{SFR_{IR}}$ by the mean $\mathrm{SFR_{UV}}$. Using our bootstrap stacking results from Section 3.2, we can compute the median ratio and errors (68%) on the obscured and UV luminous SFRs to be $0.6^{+0.4}_{-0.3}$ and $0.7^{+0.2}_{-0.3}$, respectively. This suggests that unobscured SFRs measured from the rest-frame UV data should be corrected by factors of $1.6^{+0.4}_{-0.3}$ ($0.20^{+0.10}_{-0.10}$ dex) for $z \sim 7$ and $1.7^{+0.2}_{-0.3}$ ($0.23^{+0.06}_{-0.09}$ dex) for $z \sim 8$.

We can illustrate the impact these corrections have on the estimated SFR densities at $z \sim 7$–8 from UV-bright galaxies based on the UV luminosity functions (LFs) derived by Bouwens et al. (2015) and Stefanon et al. (2019) integrated down to -21.5 mag ($\sim 1.7\ L^{*}_{\mathrm{UV}}$). Applying these corrections to the UV luminosity density that Bouwens et al. (2015) derived at $z \sim 7$ and Stefanon et al. (2019) derived at $z \sim 8$, we show the impact of these corrections on the computed SFR densities at $z \sim 7$–8 in Figure 11. Our ALMA results suggest that $\sim\frac{1}{3}$ of the SFR density in $\gtrsim 1.7\ L^{*}$ galaxies is obscured by dust. This is consistent with the 20%–25% fraction of the cosmic SFR density that Zavala et al. (2021) inferred to be obscured at $z \sim 6$–7, but it is worth emphasizing that the fraction we infer is for the UV-bright $z \sim 7$ population, and the fraction Zavala et al. (2021) derived is with respect to the total.

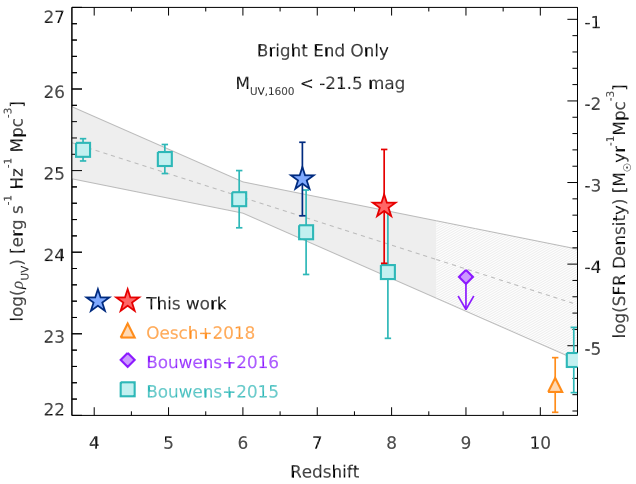

Figure 11. The SFR density inferred for especially bright ($M_{\mathrm{UV},AB} < -21.5$ mag: $\gtrsim 1.7\ L_{\mathrm{UV}}^{*}$) galaxies at $z \sim 4$–9, based on the rest-frame UV light (blue circles and squares) alone and including the contribution of dust-obscured star formation at $z \sim 7$ and $z \sim 8$ (red points). The shaded gray region indicates the best-fit trend in UV luminosity density (68% confidence intervals) for UV-bright (<-21.5 mag: $\gtrsim 1.7\ L_{\mathrm{UV}}^{*}$) galaxies against redshift (Stefanon et al. 2019). Our ALMA results suggest that $\sim$25%–50% of the star formation activity in such bright $z \sim 7$–8 galaxies is obscured by dust.

Finally, we can combine the present constraints on the IR luminosities of sources with the $z \sim 7$–8 rest-frame UV LF results of Bowler et al. (2017) and Stefanon et al. (2019) to place constraints on the IR LF at $z > 3$ such as discussed in Koprowski et al. (2017), Casey et al. (2018), Gruppioni et al. (2020), and Zavala et al. (2021). We find that the number density of galaxies with $L_{\mathrm{IR}} > 10^{11} - 10^{12}\ L_{\odot}$ is $\gtrsim 2 \times 10^{-6}$ Mpc^{-3} dex^{-1}. This value is insensitive to the assumed dust temperature, because changing the dust temperature does not change the number of detected galaxies in the range $L_{\mathrm{IR}} > 10^{11} - 10^{12}\ L_{\odot}$.

The $\gtrsim 2 \times 10^{-6}$ Mpc^{-3} dex^{-1} lower limit is fairly consistent with the dust-poor model described in Casey et al. (2018), which is only $\sim$0.5 dex higher ($\sim 6 \times 10^{-6}$ Mpc^{-3} dex^{-1} at $z = 7.5$ and $L_{\mathrm{IR}} = 3 \times 10^{11}\ L_{\odot}$), while the dust-rich model is $\sim$1.7 dex higher ($\sim 1 \times 10^{-4}$ Mpc^{-3} dex^{-1} at $z = 7.5$ and $L_{\mathrm{IR}} = 3 \times 10^{11}\ L_{\odot}$). Our lower limit is $\sim$0.3 dex higher than the model presented in Zavala et al. (2021; $\sim 9 \times 10^{-7}$ Mpc^{-3} dex^{-1} at $z = 7.5$ and $L_{\mathrm{IR}} = 3 \times 10^{11}\ L_{\odot}$). Better agreement with our observational results could be obtained by increasing the volume density of $L_{\mathrm{IR}} \sim 10^{11} - 10^{12}\ L_{\odot}$ galaxies in this model by $\gtrsim 2\times$ (see also ?). Finally, our lower limit is significantly higher ($\sim$4.5 dex) than the evolution of the IR LF presented in Koprowski et al. (2017; $\sim 7 \times 10^{-11}$ Mpc^{-3} dex^{-1} at $z = 7.5$ and $L_{\mathrm{IR}} = 3 \times 10^{11}\ L_{\odot}$). The significant tension with our results is primarily derived from the fact that this model is only constrained by observations to $z \sim 5$ and the assumption of an

exponential decline of the normalization parameter (Φ_*) of the model LF to higher redshifts.

5. Summary

We describe the analysis of sensitive ALMA-continuum observations we have obtained over 15 bright Lyman-break galaxies at $z \sim 7$–8. The ALMA-continuum observations we consider (in total 25.7 hr on source) are drawn from five distinct ALMA programs (Table 1) and allow us to assess the contribution of obscured star formation to the build-up of stellar mass in these galaxies. The observations are sensitive enough to probe down to obscured SFRs of $\sim 20\ M_\odot\ \mathrm{yr}^{-1}$ (3σ). The bright Lyman-break galaxies we have targeted were drawn from a selection of the brightest $z \sim 7$–8 galaxies identified over the UltraVISTA (Stefanon et al. 2017, 2019; S. Schouws et al., in preparation) and CANDELS COSMOS field (Smit et al. 2015, 2018).

Out of the 15 $z \sim 7$–8 galaxies we target, we detect six in the dust continuum, with inferred IR luminosities ranging from $2.7 \times 10^{11}\ L_\odot$ to $1.1 \times 10^{12}\ L_\odot$, with a median of $3.5 \times 10^{11}\ L_\odot$. This is equivalent to obscured SFRs of 25 to 101 $M_\odot\ \mathrm{yr}^{-1}$ (Figure 1). These dust detections more than double the number of normal star-forming galaxies at $z > 6.5$, which are detected in the IR continuum from four (Watson et al. 2015; Laporte et al. 2017; Bowler et al. 2018; Hashimoto et al. 2019; Tamura et al. 2019) to 10 (Figure 2). We find the spatial position of dust-continuum detections to be approximately co-spatial with the rest-frame UV light (median offset $<0.2''$), with UVISTA-Y-003 being a notable exception. For UVISTA-Y-003, the dust-continuum detection is offset by $\sim 0.3''$ from three distinct star-forming clumps seen in the rest-frame UV (Figure 5).

Using the new dust-continuum detections, we can quantify the relative contribution that obscured and unobscured star formation provide to bright galaxies at $z \sim 7$–8. For the six bright galaxies in our sample that show ALMA-continuum detections, we find that obscured SFR in these galaxies is comparable to the unobscured SFR in the median (Figure 3). The relation between SFR and $[\mathrm{C\ II}]_{158\mu\mathrm{m}}$ luminosity, for those sources with a $[\mathrm{C\ II}]_{158\mu\mathrm{m}}$ detection, will be explored in S. Schouws et al. (2021, in preparation).

We also use our observations to look at the measured IRX ($L_{\mathrm{IR}}/L_{\mathrm{UV}}$) in these galaxies and quantify how the IRX depends on the UV-continuum slope β_{UV} and the stellar mass. The IRX is well known to correlate with both quantities, but there continues to be significant debate regarding the precise trend at $z > 6$ with both β_{UV} and stellar mass.

Our IRX against β_{UV} results show a significant dependence on what we assume for the dust temperature of $z \sim 7$–8 galaxies as well as what we assume for the unreddened UV slope $\beta_{\mathrm{UV,intr}}$ for star-forming galaxies at $z \sim 7$–8. If we adopt a modified blackbody SED with a dust temperature of 50 K and an opacity index $\beta = 1.6$ as our fiducial far-IR SED, we find current IRX against β results are most consistent with an SMC dust curve if $\beta_{\mathrm{UV,intr}} = -2.63$ and lie somewhere between a Calzetti and SMC dust curve if $\beta_{\mathrm{UV,intr}} = -2.23$ (Figure 6). Adopting the same fiducial SEDs for interpreting IRX trends with stellar mass, we find results (Figure 8) that are consistent with no evolution in the IRX–stellar mass relation from $z \sim 0$ (Whitaker et al. 2017).

Additionally, we use our new dust detections to estimate the total mass of dust in bright $z \sim 7$–8 galaxies, for dust ejected from SNe after reverse shock destruction. The dust masses we derive are dependent on the assumed dust temperature and range from $\sim 10^8 M_\odot$ for low dust temperatures ($T \sim 30$ K) to $\sim 10^7 M_\odot$ for high temperatures ($T \sim 60$ K; Figure 10). Combining these dust masses with the estimates for the stellar mass from SED fitting enables constraints on dust formation mechanisms (following Michałowski 2015). This shows that our observed dust masses could most likely be explained by dust production from SNe with low dust destruction (less than $\sim$90%; see bottom panel of Figure 10).

The new measurements we make of the obscured SFRs in bright $z \sim 7$–8 allow us to improve our estimates of the contribution that very luminous bright galaxies make to the SFR density at $z \sim 7$–8. Incorporating the contribution from obscured star formation for both our bright $M_{\mathrm{UV},AB} < -21.5$ ($\gtrsim 1.7 L^*_{\mathrm{UV}}$) $z \sim 7$ and $z \sim 8$ sample to the unobscured SFRs in these galaxies, we measure correction factors of $1.6^{+0.4}_{-0.3}$ ($0.20^{+0.10}_{-0.10}$ dex) and $1.7^{+0.2}_{-0.3}$ ($0.23^{+0.06}_{-0.09}$ dex), respectively. These results clearly illustrate the important role that obscured star formation can play in the early stellar mass build-up of galaxies at $z \geqslant 7$.

Finally, we use these results to set a lower limit on the IR LF of $z \sim 7$–8 galaxies, finding $\gtrsim 2 \times 10^{-6}\ \mathrm{Mpc}^{-3}\ \mathrm{dex}^{-1}$ for galaxies with $L_{\mathrm{IR}} > 10^{11} - 10^{12}\ L_\odot\ \mathrm{yr}^{-1}$. This limit is most consistent with the dust-poor model of Casey et al. (2018), which is $\sim$0.5 dex higher.

In the future, we expect a significant increase in the number of dust-detected galaxies in normal star-forming galaxies at $z \sim 7$–8 from the ongoing ALMA observations from the Reionization Era Bright Emission Line Survey (REBELS) ALMA Large program (2019.1.01634.L). This should allow us to look at the build-up of dust in massive galaxies in much more detail, while allowing for a much more detailed look into how the measured IRX depends on both stellar mass and the UV slope.

We are greatly appreciative to our ALMA program coordinators Daniel Harsono and Carmen Toribio at ALLEGRO for support with our ALMA programs. This paper makes use of the following ALMA data: ADS/JAO.ALMA#2017.1.01217.S, ADS/JAO.ALMA#2017.1.00604.S, ADS/JAO.ALMA#2018.1.00236.S, ADS/JAO.ALMA#2018.1.00085.S and ADS/JAO.ALMA#2018.A.00022.S. ALMA is a partnership of ESO (representing its member states), NSF (USA) and NINS (Japan), together with NRC (Canada), MOST and ASIAA (Taiwan), and KASI (Republic of Korea), in cooperation with the Republic of Chile. The Joint ALMA Observatory is operated by ESO, AUI/NRAO and NAOJ. S.S., M.S., and R.B. acknowledge support from TOP grant TOP1.16.057 and a NOVA (Nederlandse Onderzoekschool Voor Astronomie) 5 grant. R.S. acknowledges support from an STFC Ernest Rutherford Fellowship (ST/S004831/1). J.H. acknowledges support of the VIDI research program with project No. 639.042.611, which is (partly) financed by the Netherlands Organisation for Scientific Research (NWO). S.C. acknowledges support from the European Research Council No. 74120 INTERSTELLAR. R.M. acknowledges support by the Science and Technology Facilities Council (STFC) and ERC Advanced grant 695671 "QUENCH."

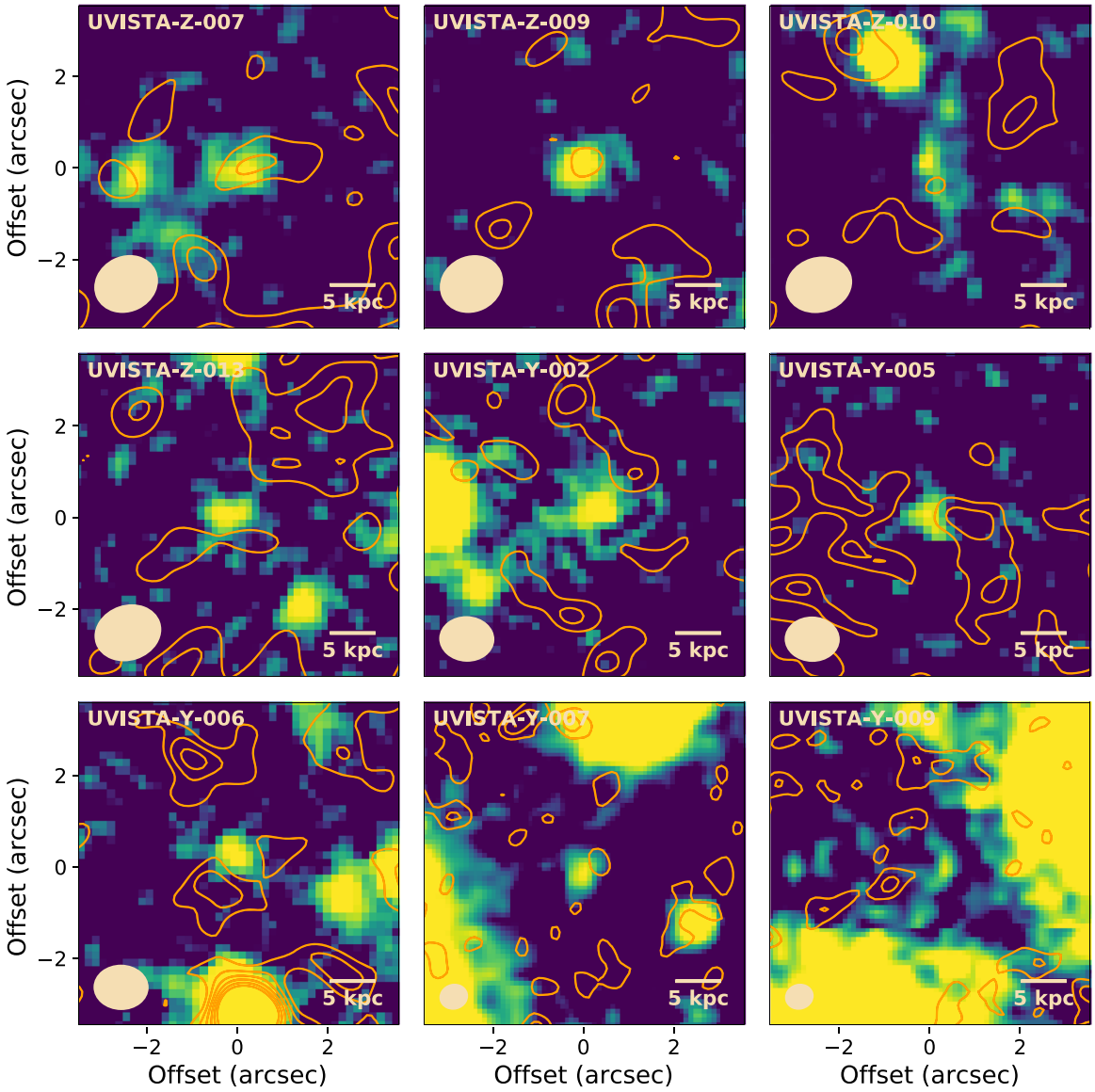

Figure 12. Dust-continuum observations (1.2 μm) overlaid on the available NIR imaging observations from UltraVISTA (stacked J+H+K$_s$). Shown are the nine $z\sim7$–8 sources that were not detected in the dust continuum. Contours are drawn at (1, 2, 3, 4, 5, 6) $\times\,\sigma$ where $\sigma\approx15$ μJy beam^{-1}. The synthesized beam for the dust-continuum observations is indicated in the lower-left corner of each panel.

Appendix A
ALMA Observations of Bright $z\sim7$–8 Galaxies That Are Undetected in the Dust Continuum

Nine of the 15 bright $z\sim7$–8 galaxies (60%) targeted by the ALMA programs considered here did not show 3σ detections in the dust continuum. Figure 12 shows rest-frame UV images of those nine sources along with 1σ, 2σ, 3σ, 4σ, and 5σ contours showing the IR dust-continuum emission. Interestingly enough, in the observations we obtain of UVISTA-Y-006, one foreground galaxy in our ALMA beam shows a clear dust-continuum detection (lowest row in Figure 12, left panel).

Appendix B
Briggs Weighted Imaging of the Continuum Detected Sources

Figure 13 shows the Briggs weighted imaging of those targets from our programs with a continuum detection. Briggs weighting changes the relative contributions of long baselines and shorter baselines in the *(u,v)*-plane, which affects the point-spread function and subsequently the effective resolution and signal-to-noise of our observations. The trade-off for increasing the resolution is a decrease in signal-to-noise. The Briggs weighting is parameterized using the *robust* parameter (R), which varies from -2.0 to $+2.0$. A value of $R=-2.0$ is equivalent to a uniform weighting, which has the highest resolution but lowest S/N and $R=+2.0$, which is equivalent to natural weighting, corresponding to the lowest resolution and highest S/N.

In Figure 13, we use the lowest robust parameter that still results in a $\geqslant3\sigma$ peak flux (in steps of $\Delta R=0.2$). Note that due to the loss in signal-to-noise caused by the Briggs weighting, the contours only show the location of the peak of the dust emission, not its extent. For all detections, clear overlap is seen between the dust-continuum and rest-frame UV emission.

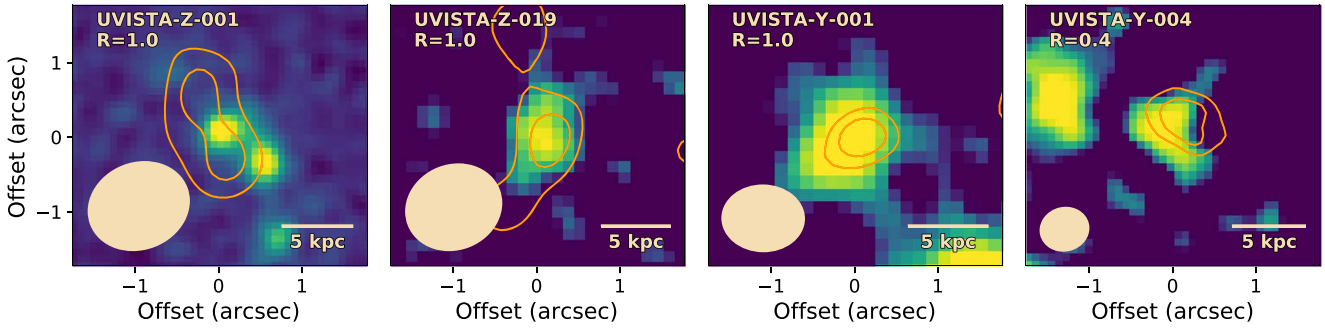

Figure 13. The Briggs weighted dust-continuum imaging (orange contours) overlaid on the rest-frame UV imaging (HST F140W for UVISTA-Z-001, ground-based J+H+K for the others) for four targets from our programs with continuum detections. The *robust* parameter we utilize for the imaging is also indicated for each source. We see no significant offset between the dust-continuum and rest-frame UV emission. The apparent offset ($0\farcs28$ or ~1.5 Kpc) between the UV and IR peaks for UVISTA-Y-004 is not significant, being comparable to the S/N-based astrometric accuracy ($\sim 0\farcs2$).

ORCID iDs

Sander Schouws https://orcid.org/0000-0001-9746-0924
Mauro Stefanon https://orcid.org/0000-0001-7768-5309
Rychard Bouwens https://orcid.org/0000-0002-4989-2471
Renske Smit https://orcid.org/0000-0001-8034-7802
Jacqueline Hodge https://orcid.org/0000-0001-6586-8845
Ivo Labbé https://orcid.org/0000-0002-2057-5376
Hiddo Algera https://orcid.org/0000-0002-4205-9567
Leindert Boogaard https://orcid.org/0000-0002-3952-8588
Stefano Carniani https://orcid.org/0000-0002-6719-380X
Yoshinobu Fudamoto https://orcid.org/0000-0001-7440-8832
Benne W. Holwerda https://orcid.org/0000-0002-4884-6756
Garth D. Illingworth https://orcid.org/0000-0002-8096-2837
Roberto Maiolino https://orcid.org/0000-0002-4985-3819
Michael Maseda https://orcid.org/0000-0003-0695-4414
Pascal Oesch https://orcid.org/0000-0001-5851-6649
Paul van der Werf https://orcid.org/0000-0001-5434-5942

References

Magnelli, Elbaz, D., Chary, R. R., et al. 2009, A&A, 496, 57
Laporte, Pelló, R., Hayes, M., et al. 2012, A&A, 542, L31
Álvarez-Márquez, J., Burgarella, D., Heinis, S., et al. 2016, A&A, 587, A122
Aravena, M., Boogaard, L., Go´nzalez-Lo´pez, J., et al. 2020, ApJ, 901, 79
Aravena, M., Decarli, R., Walter, F., et al. 2016, ApJ, 833, 68
Ashby, M. L. N., Caputi, K. I., Cowley, W., et al. 2018, ApJS, 237, 39
Bakx, T. J. L. C., Tamura, Y., Hashimoto, T., et al. 2020, MNRAS, 493, 4294
Bañados, E., Decarli, R., Walter, F., et al. 2015, ApJL, 805, L8
Barisic, I., Faisst, A. L., Capak, P. L., et al. 2017, ApJ, 845, 41
Behrens, C., Pallottini, A., Ferrara, A., Gallerani, S., & Vallini, L. 2018, MNRAS, 477, 552
Béthermin, M., Daddi, E., Magdis, G., et al. 2015, A&A, 573, A113
Béthermin, M., Fudamoto, Y., Ginolfi, M., et al. 2020, A&A, 643, A2
Béthermin, M., Wu, H.-Y., Lagache, G., et al. 2017, A&A, 607, A89
Bianchi, S., & Schneider, R. 2007, MNRAS, 378, 973
Bouwens, R., González-López, J., Aravena, M., et al. 2020, ApJ, 902, 112
Bouwens, R. J., Aravena, M., Decarli, R., et al. 2016b, ApJ, 833, 72
Bouwens, R. J., Bradley, L., Zitrin, A., et al. 2014, ApJ, 795, 126
Bouwens, R. J., Illingworth, G. D., Oesch, P. A., et al. 2011, ApJ, 737, 90
Bouwens, R. J., Illingworth, G. D., Oesch, P. A., et al. 2015, ApJ, 803, 34
Bouwens, R. J., Oesch, P. A., Illingworth, G. D., Ellis, R. S., & Stefanon, M. 2017, ApJ, 843, 129
Bouwens, R. J., Oesch, P. A., Labbé, I., et al. 2016a, ApJ, 830, 67
Bowler, R. A. A., Bourne, N., Dunlop, J. S., McLure, R. J., & McLeod, D. J. 2018, MNRAS, 481, 1631
Bowler, R. A. A., Dunlop, J. S., McLure, R. J., & McLeod, D. J. 2017, MNRAS, 466, 3612
Bradač, M., Garcia-Appadoo, D., Huang, K.-H., et al. 2017, ApJL, 836, L2
Calzetti, D., Armus, L., Bohlin, R. C., et al. 2000, ApJ, 533, 682
Capak, P., Aussel, H., Ajiki, M., et al. 2007, ApJS, 172, 99
Capak, P., Aussel, H., Bundy, K., et al. 2013, Spitzer Proposal 90042
Capak, P. L., Carilli, C., Jones, G., et al. 2015, Natur, 522, 455
Caputi, K. I., Deshmukh, S., Ashby, M. L. N., et al. 2017, ApJ, 849, 45
Carniani, S., Maiolino, R., Pallottini, A., et al. 2017, A&A, 605, A42
Carniani, S., Maiolino, R., Smit, R., & Amorín, R. 2018, ApJL, 854, L7
Casey, C. M. 2012, MNRAS, 425, 3094
Casey, C. M., Scoville, N. Z., Sanders, D. B., et al. 2014, ApJ, 796, 95
Casey, C. M., Zavala, J. A., Spilker, J., et al. 2018, ApJ, 862, 77
Cazaux, S., & Tielens, A. G. G. M. 2004, ApJ, 604, 222
Chabrier, G. 2003, PASP, 115, 763
Chen, L.-H., Hirashita, H., Hou, K.-C., et al. 2017, MNRAS, 474, 1545
Cherchneff, I., & Dwek, E. 2010, ApJ, 713, 1
Clark, C. J. R., De Vis, P., Baes, M., et al. 2019, MNRAS, 489, 5256
Coppin, K. E. K., Geach, J. E., Almaini, O., et al. 2014, MNRAS, 446, 1293
Cormier, D., Abel, N. P., Hony, S., et al. 2019, A&A, 626, A23
Cucciati, O., Tresse, L., Ilbert, O., et al. 2012, A&A, 539, A31
da Cunha, E., Groves, B., Walter, F., et al. 2013, ApJ, 766, 13
Daddi, E., Dannerbauer, H., Stern, D., et al. 2009, ApJ, 694, 1517
Daddi, E., Dickinson, M., Morrison, G., et al. 2007, ApJ, 670, 156
Dunlop, J. S., McLure, R. J., Biggs, A. D., et al. 2016, MNRAS, 466, 861
Ellis, R. S., McLure, R. J., Dunlop, J. S., et al. 2012, ApJL, 763, L7
Endsley, R., Stark, D. P., Chevallard, J., & Charlot, S. 2021, MNRAS, 500, 5229
Erben, T., Hildebrandt, H., Lerchster, M., et al. 2009, A&A, 493, 1197
Faisst, A. L., Capak, P. L., Yan, L., et al. 2017, ApJ, 847, 21
Faisst, A. L., Fudamoto, Y., Oesch, P. A., et al. 2020, ApJS, 247, 61
Ferrara, A., & Peroux, C. 2021, MNRAS, 503, 4537
Ferrarotti, A. S., & Gail, H. P. 2006, A&A, 447, 553
Finkelstein, S. L., Ryan, R. E., Papovich, C., et al. 2015, ApJ, 810, 71
Fudamoto, Y., Oesch, P. A., Faisst, A., et al. 2020, A&A, 643, A4
Fudamoto, Y., Oesch, P. A., Magnelli, B., et al. 2019, MNRAS, 491, 4724
Fudamoto, Y., Oesch, P. A., Schinnerer, E., et al. 2017, MNRAS, 472, 483
Gaia Collaboration, Brown, A. G. A., Vallenari, A., et al. 2018, A&A, 616, A1
Gall, C., Hjorth, J., & Andersen, A. C. 2011, A&ARv, 19, 43
Gould, R. J., & Salpeter, E. E. 1963, ApJ, 138, 393
Grogin, N. A., Kocevski, D. D., Faber, S. M., et al. 2011, ApJS, 197, 35
Gruppioni, C., Béthermin, M., Loiacono, F., et al. 2020, A&A, 643, A8
Harikane, Y., Ouchi, M., Inoue, A. K., et al. 2020, ApJ, 896, 93
Hashimoto, T., Inoue, A. K., Mawatari, K., et al. 2019, PASJ, 71, 71
Hashimoto, T., Laporte, N., Mawatari, K., et al. 2018, Natur, 557, 392
Hildebrandt, H., Pielorz, J., Erben, T., et al. 2009, A&A, 498, 725
Hirashita, H., & Ferrara, A. 2002, MNRAS, 337, 921
Hirashita, H., Ferrara, A., Dayal, P., & Ouchi, M. 2014, MNRAS, 443, 1704
Hodge, J. A., & da Cunha, E. 2020, RSOS, 7, 200556
Inoue, A. K., Tamura, Y., Matsuo, H., et al. 2016, Sci, 352, 1559
Karim, A., Schinnerer, E., Martínez-Sansigre, A., et al. 2011, ApJ, 730, 61
Kawamata, R., Ishigaki, M., Shimasaku, K., et al. 2018, ApJ, 855, 4
Knudsen, K. K., Watson, D., Frayer, D., et al. 2017, MNRAS, 466, 138
Koprowski, M. P., Dunlop, J. S., Michałowski, M. J., et al. 2017, MNRAS, 471, 4155
Lakićević, M., van Loon, J. T., Meixner, M., et al. 2015, ApJ, 799, 50
Laporte, N., Ellis, R. S., Boone, F., et al. 2017, ApJL, 837, L21
Laporte, N., Katz, H., Ellis, R. S., et al. 2019, MNRAS, 487, L81

Le Fèvre, O., Béthermin, M., Faisst, A., et al. 2020, A&A, 643, A1
Leśniewska, A., & Michałowski, M. J. 2019, A&A, 624, L13
Liang, L., Feldmann, R., Kereš, D., et al. 2019, MNRAS, 489, 1397
Madau, P., & Dickinson, M. 2014, ARA&A, 52, 415
Magnelli, Boogaard, L., Decarli, R., et al. 2020, ApJ, 892, 66
Magnelli, Popesso, P., Berta, S., et al. 2013, A&A, 553, A132
Maiolino, R., Carniani, S., Fontana, A., et al. 2015, MNRAS, 452, 54
Marrone, D. P., Spilker, J. S., Hayward, C. C., et al. 2018, Natur, 553, 51
Martí-Vidal, I., Vlemmings, W. H. T., Muller, S., & Casey, S. 2014, A&A, 563, A136
Matthee, J., Sobral, D., Boogaard, L. A., et al. 2019, ApJ, 881, 124
Matthee, J., Sobral, D., Boone, F., et al. 2017, ApJ, 851, 145
Mazzucchelli, C., Bañados, E., Venemans, B. P., et al. 2017, ApJ, 849, 91
McCracken, H. J., Milvang-Jensen, B., Dunlop, J., et al. 2012, A&A, 544, A156
McLeod, D. J., McLure, R. J., & Dunlop, J. S. 2016, MNRAS, 459, 3812
McLure, R. J., Dunlop, J. S., Bowler, R. A. A., et al. 2013, MNRAS, 432, 2696
McLure, R. J., Dunlop, J. S., Cullen, F., et al. 2018, MNRAS, 476, 3991
Meurer, G. R., Heckman, T. M., & Calzetti, D. 1999, ApJ, 521, 64
Michałowski, M., Hjorth, J., & Watson, D. 2010, A&A, 514, A67
Michałowski, M. J. 2015, A&A, 577, A80
Momcheva, I. G., van Dokkum, P. G., van der Wel, A., et al. 2016, PASP, 129, 015004
Morgan, H. L., & Edmunds, M. G. 2003, MNRAS, 343, 427
Nanni, A., Bressan, A., Marigo, P., & Girardi, L. 2014, MNRAS, 438, 2328
Nozawa, T., Kozasa, T., Umeda, H., Maeda, K., & Nomoto, K. 2003, ApJ, 598, 785
Oesch, P. A., Bouwens, R. J., Illingworth, G. D., et al. 2014, ApJ, 786, 108
Oesch, P. A., Bouwens, R. J., Illingworth, G. D., et al. 2015, ApJ, 808, 104
Oesch, P. A., Bouwens, R. J., Illingworth, G. D., Labbé, I., & Stefanon, M. 2018, ApJ, 855, 105
Oke, J. B., & Gunn, J. E. 1983, ApJ, 266, 713
Omukai, K. 2000, ApJ, 534, 809
Omukai, K., Tsuribe, T., Schneider, R., & Ferrara, A. 2005, ApJ, 626, 627
Ota, K., Walter, F., Ohta, K., et al. 2014, ApJ, 792, 34
Oteo, I., Ivison, R. J., Dunne, L., et al. 2016, ApJ, 827, 34
Overzier, R. A., Heckman, T. M., Wang, J., et al. 2010, ApJL, 726, L7
Pannella, M., Elbaz, D., Daddi, E., et al. 2015, ApJ, 807, 141
Pentericci, L., Carniani, S., Castellano, M., et al. 2016, ApJL, 829, L11
Reddy, N., Dickinson, M., Elbaz, D., et al. 2011, ApJ, 744, 154
Reddy, N. A., Erb, D. K., Pettini, M., Steidel, C. C., & Shapley, A. E. 2010, ApJ, 712, 1070
Reddy, N. A., Oesch, P. A., Bouwens, R. J., et al. 2018, ApJ, 853, 56
Reddy, N. A., Steidel, C. C., Fadda, D., et al. 2006, ApJ, 644, 792
Rémy-Ruyer, A., Madden, S. C., Galliano, F., et al. 2015, A&A, 582, A121
Riechers, D. A., Bradford, C. M., Clements, D. L., et al. 2013, Natur, 496, 329
Roberts-Borsani, G. W., Bouwens, R. J., Oesch, P. A., et al. 2016, ApJ, 823, 143
Roberts-Borsani, G. W., Ellis, R. S., & Laporte, N. 2020, MNRAS, 497, 3440
Rossi, M. E. D., Rieke, G. H., Shivaei, I., Bromm, V., & Lyu, J. 2018, ApJ, 869, 4
Salim, S., & Narayanan, D. 2020, ARA&A, 58, 529
Schaerer, D., & de Barros, S. 2009, A&A, 502, 423
Schenker, M. A., Robertson, B. E., Ellis, R. S., et al. 2013, ApJ, 768, 196
Schneider, R., Omukai, K., Inoue, A. K., & Ferrara, A. 2006, MNRAS, 369, 1437
Schneider, R., Valiante, R., Ventura, P., et al. 2014, MNRAS, 442, 1440
Schreiber, C., Elbaz, D., Pannella, M., et al. 2018, A&A, 609, A30
Schreiber, C., Pannella, M., Elbaz, D., et al. 2015, A&A, 575, A74
Scoville, N., Aussel, H., Brusa, M., et al. 2007, ApJS, 172, 1
Siana, B., Teplitz, H. I., Chary, R.-R., Colbert, J., & Frayer, D. T. 2008, ApJ, 689, 59
Sklias, P., Zamojski, M., Schaerer, D., et al. 2014, A&A, 561, A149
Smail, I., Geach, J. E., Swinbank, A. M., et al. 2014, ApJ, 782, 19
Smit, R., Bouwens, R. J., Carniani, S., et al. 2018, Natur, 553, 178
Smit, R., Bouwens, R. J., Franx, M., et al. 2015, ApJ, 801, 122
Sommovigo, L., Ferrara, A., Carniani, S., et al. 2021, MNRAS, 503, 4878
Stefanon, M., Labbé, I., Bouwens, R. J., et al. 2017, ApJ, 851, 43
Stefanon, M., Labbé, I., Bouwens, R. J., et al. 2019, ApJ, 883, 99
Stefanon, M., Aravena, M., Bouwens, R., et al. 2021, JWST Prop., 1, 1626
Strandet, M. L., Weiss, A., Vieira, J. D., et al. 2016, ApJ, 822, 80
Takeuchi, T. T., Buat, V., Heinis, S., et al. 2010, A&A, 514, A4
Tamura, Y., Mawatari, K., Hashimoto, T., et al. 2019, ApJ, 874, 27
Todini, P., & Ferrara, A. 2001, MNRAS, 325, 726
Venemans, B. P., Bañados, E., Decarli, R., et al. 2015b, ApJL, 801, L11
Venemans, B. P., Decarli, R., Walter, F., et al. 2018, ApJ, 866, 159
Venemans, B. P., McMahon, R. G., Walter, F., et al. 2012, ApJL, 751, L25
Venemans, B. P., Walter, F., Decarli, R., et al. 2017, ApJL, 851, L8
Venemans, B. P., Walter, F., Zschaechner, L., et al. 2015a, ApJ, 816, 37
Ventura, P., Criscienzo, M. D., Schneider, R., et al. 2012, MNRAS, 424, 2345
Wang, T., Schreiber, C., Elbaz, D., et al. 2019, Natur, 572, 211
Watson, D., Christensen, L., Knudsen, K. K., et al. 2015, Natur, 519, 327
Whitaker, K. E., Pope, A., Cybulski, R., et al. 2017, ApJ, 850, 208
Williams, C. C., Labbe, I., Spilker, J., et al. 2019, ApJ, 884, 154
Willott, C. J., Carilli, C. L., Wagg, J., & Wang, R. 2015, ApJ, 807, 180
Yamasawa, D., Habe, A., Kozasa, T., et al. 2011, ApJ, 735, 44
Zavala, J. A., Casey, C. M., Manning, S. M., et al. 2021, ApJ, 909, 165